# [H(OXeF$_2$)$_n$][AsF$_6$] and [FXe$^{II}$(OXe$^{IV}$F$_2$)$_n$][AsF$_6$] ($n$ = 1, 2): Examples of Xenon(IV) Hydroxide Fluoride and Oxide Fluoride Cations and the Crystal Structures of [F$_3$Xe---FH][Sb$_2$F$_{11}$] and [H$_5$F$_4$][SbF$_6$] ·2[F$_3$Xe---FH][Sb$_2$F$_{11}$]

David S. Brock, Hélène P. A. Mercier, and Gary J. Schrobilgen*

Department of Chemistry, McMaster University, Hamilton, Ontario L8S 4M1, Canada

Ⓢ *Supporting Information*

**ABSTRACT:** The xenon(IV) hydroxide fluoride and oxide fluoride salts, [H(OXeF$_2$)$n$] [AsF$_6$] and [FXe$^{II}$(OXe$^{IV}$F$_2$)$_n$][AsF$_6$] ($n$ = 1, 2), have been synthesized as the natural abundance and the $^{18}$O- and $^2$H-enriched salts and structurally characterized by low-temperature Raman spectroscopy. Quantum-chemical calculations have been used to arrive at vibrational assignments. The experimental vibrational frequencies and isotopic shift trends are reproduced by the calculated gas-phase frequencies at several levels of theory. The cation chain is limited to one or two OXeF$_2$ subunits, which are oxygen-bridged and strongly ion-paired with the AsF$_6^-$ anion. The reaction of XeOF$_2$·$x$HF with a superacidic HF/SbF$_5$ solvent mixture yielded crystals of [H$_5$F$_4$][SbF$_6$]·2[XeF$_3$·HF]-[Sb$_2$F$_{11}$], [XeF$_3$·HF][Sb$_2$F$_{11}$], and [XeF$_3$][SbF$_6$]. The XeF$_3^+$ cations of each salt are very similar, displaying T-shaped primary coordination of xenon to three fluorine atoms (AX$_3$E$_2$ VSEPR arrangement) and a secondary contact to the fluorine atom of HF in [H$_5$F$_4$][SbF$_6$]·2[XeF$_3$·HF][Sb$_2$F$_{11}$] and [XeF$_3$·HF][Sb$_2$F$_{11}$] or to a fluorine atom of SbF$_6^-$ in [XeF$_3$][SbF$_6$]. The secondary coordination spheres of xenon in [H$_5$F$_4$][SbF$_6$]·2[XeF$_3$·HF][Sb$_2$F$_{11}$] and [XeF$_3$·HF][Sb$_2$F$_{11}$] are similar; however, the F$_3$Xe---FH$^+$ cation of the latter salt is disordered. An additional contact between the XeF$_3^+$ cation and the SbF$_6^-$ anion in [H$_5$F$_4$][SbF$_6$]·2[XeF$_3$·HF][Sb$_2$F$_{11}$] presumably alters the crystal packing sufficiently to give an ordered F$_3$Xe---FH$^+$ cation, a rare example in which HF is coordinated to a noble gas. The latter compound also provides the first documentation of the H$_5$F$_4^+$ acidium ion, which forms a zigzag F$_4$-chain terminated by SbF$_6^-$ anions. Enthalpies and Gibbs free energies of reaction obtained from Born−Fajans−Haber thermochemical cycles support the proposed decomposition pathways.
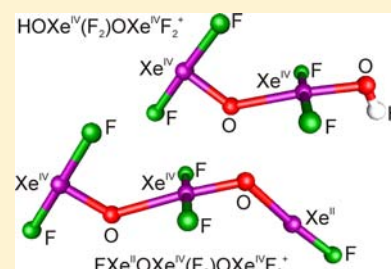
## INTRODUCTION

Although many compounds containing xenon in the +2 and +6 oxidation states are known, far fewer Xe(IV) compounds are known.[1,2] Among the factors that contribute to the relative scarcity of Xe(IV) compounds is the propensity for the oxide and oxide fluorides to undergo redox eliminations and disproportionations to Xe(II) and O$_2$, or to Xe(II) and Xe(VI).[3−6] Examples of Xe(IV) cations are presently limited to C$_6$F$_5$XeF$_2^+$,[7] XeF$_3^+$,[8−15] and F$_x$Xe(OTeF$_5$)$_{3−x}^+$ ($x$ = 0−2).[16] Although several examples of cations containing more than one xenon atom are known, namely, those of Xe(II) (Xe$_2$F$_3^+$,[8,17] Xe$_3$OF$_3^+$,[18]), Xe(VI) (Xe$_2$F$_{11}^+$,[19,20] F(O)$_2$Xe---F---Xe(O)$_2$F$^+$ [21]), and the mixed-oxidation state coordination complexes XeF$_2$·XeF$_5^+$, 2XeF$_2$·XeF$_5^+$, XeF$_2$·2XeF$_5^+$,[22] and XeF$_2$·XeF$_4$·Mg$^{2+}$,[23] polynuclear cations of Xe(IV) are unknown. All of the aforementioned polynuclear xenon cations and the Xe$_3$OF$_3^+$ cation contain fluorine-bridged xenon atoms (the Xe$_3$OF$_3^+$ cation also contains a Xe−O−Xe bridge).[18] The general preference for fluorine-bridge formation over oxygen-bridge formation is also found in the polynuclear Xe(VI) salt, [Cs][(XeOF$_4$)$_3$F].[24,25]

The only confirmed hydroxy derivatives of xenon are the perxenate anions, H$_3$XeO$_6^-$, H$_2$XeO$_6^{2-}$, and HXeO$_6^{3-}$ that were observed by conventional and stopped-flow spectrophotometry in the pH ranges −0.2−2, 6−8, and 12−13, respectively.[26] The Raman spectra of aqueous alkaline perxenate solutions show the Xe(VIII) species present are octahedrally coordinated but fail to provide further structural details.[27] Several other reports speculating on the existence of "xenic acid" (XeO$_3$·H$_2$O, H$_2$XeO$_4$, Xe(OH)$_6$)[28−32] remain unsubstantiated. To date, no other hydroxy derivatives of xenon have been reported, and none have been structurally characterized in the solid state.

Examples in which HF is coordinated to metal centers are well established and have been the subject of a review,[33] for example, [La(HF)$_2$][AsF$_6$]$_3$, [Pb(HF)][AsF$_6$]$_2$, [Ca(HF)]-[AsF$_6$]$_2$, [Cd(HF)][AsF$_6$]$_2$, [Mg(HF)$_2$][SbF$_6$]$_2$, [Ca(HF)$_2$]-[SbF$_6$]$_2$, [Hg(HF)][SbF$_6$]$_2$, [OsO$_3$F(HF)$_2$][AsF$_6$], [OsO$_3$F(HF)][SbF$_6$], [Au(HF)$_2$][SbF$_6$]$_2$·2HF, and Mg(HF)-AuF$_4$AuF$_6$. A considerable number of new examples have appeared since this review. The only example of HF coordination to xenon occurs in the crystal structure of (XeF$_5^+$)$_2$(HF$_2^-$)$_2$·HF.[34] Further examples of HF coordination

**Table 1. Values of $\Delta H$, $\Delta S$, and $\Delta G$ Calculated from Born−Fajans−Haber Thermochemical Cycles[a] for the Decomposition Reactions of $[XeOF][AsF_6]$, $[HOXeF_2][AsF_6]$, $[HOXe(F)_2OXeF_2][AsF_6]$, $[FXeOXeF_2][AsF_6]$, and $[FXeOXe(F)_2OXeF_2][AsF_6]$**

| | $\Delta H$ (kJ mol$^{-1}$) | | $\Delta S$ (J mol$^{-1}$ K$^{-1}$) | | $\Delta G$ (kJ mol$^{-1}$) | | |
|---|---|---|---|---|---|---|---|
| | 298.15 K | 194.15 K | 298.15 K | 194.15 K | 298.15 K | 194.15 K | eq |
| $[XeOF][AsF_6]_{(s)} \rightarrow [XeF][AsF_6]_{(s)} + {}^1\!/_2O_{2(g)}$ | −293.3 | −294.0 | 93.7 | 93.7 | −321.2 | −312.2 | 3 |
| $[HOXeF_2][AsF_6]_{(s)} \rightarrow [XeF][AsF_6]_{(s)} + {}^1\!/_2O_{2(g)} + HF_{(l)}$ | −146.9 | −259.9 | 242.1 | 143.7 | −219.1 | −287.8 | 4 |
| $3[HOXe(F)_2OXeF_2][AsF_6]_{(s)} + 3H_2O_{(l)} \rightarrow 2[Xe_3OF_3][AsF_6]_{(s)} + 3O_{2(g)} + 6HF_{(l)} + [H_3O][AsF_6]_{(s)}$ | −1845.5 | −1326.8 | 1341.5 | 817.3 | −2245.5 | −1485.5 | 6 |
| $[HOXe(F)_2OXeF_2][AsF_6]_{(s)} \rightarrow [Xe_2F_3][AsF_6]_{(s)} + O_{2(g)} + HF_{(l)}$ | −549.9 | −421.1 | 362.7 | 264.3 | −658.0 | −472.4 | 7 |
| $[FXeOXeF_2][AsF_6]_{(s)} \rightarrow [Xe_2F_3][AsF_6]_{(s)} + {}^1\!/_2O_{2(g)}$ | −202.6 | −205.7 | 120.6 | 120.6 | −238.6 | −229.1 | 11 |
| $[FXeOXe(F)_2OXeF_2][AsF_6]_{(s)} \rightarrow [Xe_2F_3][AsF_6]_{(s)} + O_{2(g)} + XeF_{2(s)}$ | −544.1 | −385.1 | 242.4 | 242.4 | −616.4 | −432.2 | 12 |
| $3[FXeOXeF_2][AsF_6]_{(s)} + 3H_2O_{(l)} \rightarrow 2[Xe_3OF_3][AsF_6]_{(s)} + {}^3\!/_2O_{2(g)} + 3HF_{(l)} + [H_3O][AsF_6]_{(s)}$ | −611.3 | −670.4 | 615.3 | 386.2 | −794.8 | −745.4 | 13 |
| $[FXeOXe(F)_2OXeF_2][AsF_6]_{(s)} + H_2O_{(l)} \rightarrow [Xe_3OF_3][AsF_6]_{(s)} + O_{2(g)} + 2HF_{(l)}$ | −630.4 | −438.6 | 446.6 | 271.9 | −763.2 | −491.4 | 14 |

[a]Values reported in this table were arrived at using literature and calculated values for thermodynamic quantities as outlined in the Supporting Information (Thermochemistry).

to main-group centers are provided by the series of $H_{n+1}F_n^+$ ($n \geq 1$) acidium ions formed in the superacid medium, HF/SbF$_5$. Several acidium ion salts have been proposed for the HF/SbF$_5$ superacid system based on phase diagrams,[35] that is, $[H_2F]$-$[Sb_2F_{11}]$, $[H_3F_2][Sb_2F_{11}]$, $[H_2F][SbF_6]$, $[H_3F_2][SbF_6]$, $[H_4F_3]$-$[SbF_6]$, and $[H_7F_6][SbF_6]$, but only $[H_2F][Sb_2F_{11}]$,[36] $[H_3F_2]$-$[Sb_2F_{11}]$,[36] and $[H_7F_6][SbF_6]$[35] have thus far been isolated and structurally characterized by single-crystal X-ray diffraction.

The syntheses and structural characterizations of five new Xe(IV) cations derived from HF/AsF$_5$ and HF/SbF$_5$ superacid media are described in the present paper, which provide the first examples of isolable hydroxy derivatives of xenon, as well as rare examples of Xe(II)/Xe(IV) mixed-oxidation state compounds and HF coordinated to xenon. Quantum-chemical calculations and $^{1/2}$H- and $^{16/18}$O-enrichment studies have been employed to assign the Raman spectra of the aforementioned cations and to aid in understanding their chemical bonding.

## ■ RESULTS AND DISCUSSION

**Syntheses, Properties, and Reactivities of Salts of the $HOXeF_2^+$, $HOXe(F_2)OXeF_2^+$, $FXe^{II}OXe^{IV}F_2^+$, $FXe^{II}OXe^{IV}(F)_2OXe^{IV}F_2^+$, and $F_3Xe\text{---}FH^+$ Cations.** The reactions and the purities of all products were routinely monitored by recording the low-temperature Raman spectra (−150 °C) of the natural abundance, $^{18}$O-enriched (97.8 atom %), and $^2$H-enriched (99.5 atom %) reactants and products.
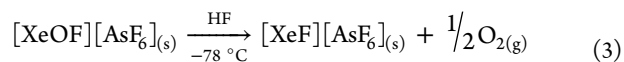
*[HOXeF$_2$][AsF$_6$]*. The title salt was obtained by the low-temperature reaction of XeOF$_2$·$n$HF ($n$ is likely 1, and HF is hydrogen bonded to oxygen)[3] with an AsF$_5$ solution in anhydrous HF (aHF) according to eq 1:

$$XeOF_2 \cdot nHF + AsF_5 \xrightarrow[-78\,°C]{HF} [HOXeF_2][AsF_6] + (n-1)HF \tag{1}$$
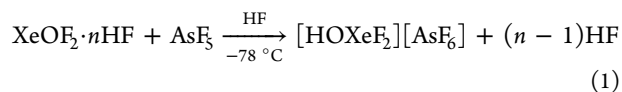
Although the reaction proceeds to a significant degree, within several minutes with only slight agitation, the reaction mixture was allowed to stand at −78 °C for 12 h to ensure complete reaction. Hydrogen fluoride and residual AsF$_5$ were removed from the resulting insoluble white solid under dynamic vacuum at −78 °C, yielding [HOXeF$_2$][AsF$_6$] as a friable, white powder.

Prior to reaction with AsF$_5$, it was necessary to ensure that XeOF$_2$, which had been prepared from its F$_2$OXeNCCH$_3$ adduct,[3] had been fully solvated to form the HF complex and had not been suspended in HF as partially solvated or

unsolvated XeOF$_2$. The slow rate of XeOF$_2$ solvation has been verified by low-temperature Raman spectroscopy and can require from 12 to 72 h at −78 °C to go to completion.[3] In a prior computational study, the HF molecule of XeOF$_2$·HF was shown to hydrogen bond to oxygen,[3] providing a more fluorobasic site for AsF$_5$ to attack and form HOXeF$_2^+$. Incomplete solvation (i.e., a mixture of XeOF$_2$·$n$HF and XeOF$_2$) resulted in extensive decomposition to [XeF][AsF$_6$] upon AsF$_5$ addition. The observation of XeF$^+$ suggests that the reaction likely proceeds through the formation of the unstable XeOF$^+$ cation (eq 2), which decomposes to O$_2$ and XeF$^+$ (eq 3):

$$XeOF_2 + AsF_5 \xrightarrow[-78\,°C]{HF} [XeOF][AsF_6]_{(s)} \tag{2}$$

$$[XeOF][AsF_6]_{(s)} \xrightarrow[-78\,°C]{HF} [XeF][AsF_6]_{(s)} + {}^1\!/_2O_{2(g)} \tag{3}$$

This reaction pathway is also consistent with the large negative $\Delta G_{194.15}$ value of eq 3 (−312.2 kJ mol$^{-1}$, Table 1) obtained from a Born−Fajans−Haber thermochemical cycle using available experimental and calculated thermodynamic parameters and values derived from volume-based thermodynamics.[37−40] The calculated exothermicity is also consistent with the explosive nature of solid XeOF$_2$ when it reacts with liquid AsF$_5$ at −78 °C.[41]

Solid [HOXeF$_2$][AsF$_6$] is stable indefinitely at −78 °C in the absence of moisture but outgases rapidly, but not explosively, upon warming to −35 °C. The resulting opaque, white coating remaining on the reactor walls was shown by Raman spectroscopy to be [XeF][AsF$_6$]. It is likely the hydroxy salt decomposes according to eq 4 ($\Delta G_{194.15}$ = −287.8 kJ mol$^{-1}$; Table 1):

$$[HOXeF_2][AsF_6]_{(s)} \rightarrow [XeF][AsF_6]_{(s)} + {}^1\!/_2O_{2(g)} + HF_{(l)} \tag{4}$$
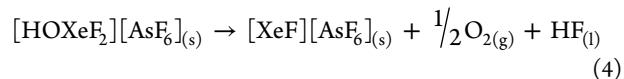
Attempts to dissolve [HOXeF$_2$][AsF$_6$] in aHF were unsuccessful. Warming a suspension of [HOXeF$_2$][AsF$_6$] to −40 °C in aHF showed no apparent solubility. Raman spectroscopy (−150 °C) confirmed that complete decomposition to [XeF][AsF$_6$] had occurred. A suspension of [HOXeF$_2$][AsF$_6$] in liquid AsF$_5$ that had been warmed to −40 °C showed the onset of decomposition to [XeF][AsF$_6$] but no xenon-containing intermediate product(s) or appreciable solubility were observed. Dissolution in the superacidic

medium HF/AsF$_5$ (1:3 v/v mixture) was also attempted. On warming to −56 °C, no solubility was apparent, with the compound decomposing to [XeF][AsF$_6$] upon further warming to −50 °C.

In an attempt to isolate [HOXeF$_2$][AsF$_6$] that is free of [XeF][AsF$_6$], half an equivalent of AsF$_5$ was allowed to react with XeOF$_2$·$n$HF for 12 h in aHF at −78 °C. Instead of pale yellow [HOXeF$_2$][AsF$_6$], the product was a br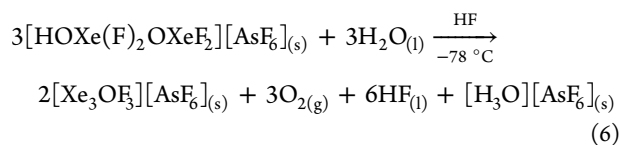ight yellow solid having a Raman spectrum that was consistent with the mixed-oxidation state salt, [FXe$^{II}$OXe$^{IV}$F$_2$][AsF$_6$] (vide infra).

*[HOXe(F)$_2$OXeF$_2$][AsF$_6$].* When XeOF$_2$·$n$HF samples had been allowed to stand for approximately 3 weeks at −78 °C under aHF, traces of water apparently diffused through the FEP reactor walls. Reaction of these samples with 0.5 equiv of AsF$_5$ for 12 h at −78 °C resulted in bright yellow solids that were consistent with the formation of [HOXe(F)$_2$OXeF$_2$][AsF$_6$]. The role of water was confirmed when the salt was synthesized by reaction of equimolar amounts of XeOF$_2$·$n$HF, H$_2$O, and AsF$_5$ in aHF at −78 °C. However, the most efficient synthesis of [HOXe(F)$_2$OXeF$_2$][AsF$_6$] resulted from the reaction of 0.5 equiv of [H$_3$O][AsF$_6$] with XeOF$_2$·$n$HF in aHF at −78 °C (eq 5):

$$2XeOF_2 \cdot nHF + [H_3O][AsF_6] \xrightarrow[-78\,°C]{HF}$$
$$[HOXe(F)_2OXeF_2][AsF_6] + H_2O_{(HF)} + 2nHF \quad (5)$$
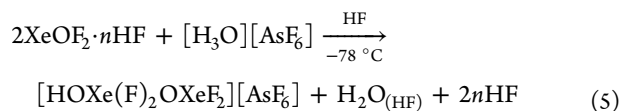
Although the aforementioned reactions are essentially the same because H$_2$O forms [H$_3$O][AsF$_6$] in the presence of AsF$_5$ and HF, the direct use of room-temperature-stable [H$_3$O][AsF$_6$] afforded more precise molar ratios for the reactants. Raman spectra of the solid products were recorded under frozen HF. Reaction of a 4:1 molar ratio of XeOF$_2$·$n$HF/[H$_3$O][AsF$_6$] resulted in a mixture of XeOF$_2$·$n$HF and [HOXe(F)$_2$OXeF$_2$]-[AsF$_6$] whereas 2:1 and 1:1 molar ratios resulted in only [HOXe(F)$_2$OXeF$_2$][AsF$_6$]. In the case of a 1:1 molar ratio, unreacted [H$_3$O][AsF$_6$] presumably remained dispersed in frozen HF and could not be observed in the Raman spectrum. Oxygen isotope scrambling was not observed when Xe$^{18}$OF$_2$·$n$HF reacted with [H$_3$$^{16}$O][AsF$_6$], producing only [H$^{18}$OXe(F)$_2$$^{18}$OXeF$_2$][AsF$_6$], thus indicating that H$_3$O$^+$ is only involved in protonation and is not otherwise involved in the reaction pathway.
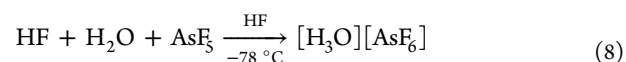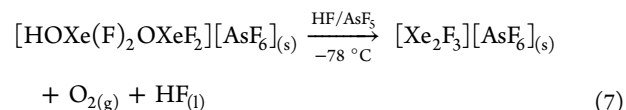
Precipitated [HOXe(F)$_2$OXeF$_2$][AsF$_6$] was stable when stored under liquid HF for several days at −78 °C. Over the course of one month at −78 °C, the supernatants of these samples deposited deep red-orange crystals that were shown by Raman spectroscopy and unit cell determinations of several crystals to be [Xe$_3$OF$_3$][AsF$_6$].[18] Evolution of a gas, which was noncondensable at −196 °C, was also observed, implying that HOXe(F)$_2$OXeF$_2$$^+$ decomposed to a Xe(II) intermediate (XeF$_2$ and/or XeF$^+$) with the release of O$_2$. The Xe(II) intermediate then reacted with water (eq 6) remaining from the synthesis of [HOXe(F)$_2$OXeF$_2$][AsF$_6$] (eq 5):

$$3[HOXe(F)_2OXeF_2][AsF_6]_{(s)} + 3H_2O_{(l)} \xrightarrow[-78\,°C]{HF}$$
$$2[Xe_3OF_3][AsF_6]_{(s)} + 3O_{2(g)} + 6HF_{(l)} + [H_3O][AsF_6]_{(s)} \quad (6)$$

The same decomposition products were observed when [HOXe(F)$_2$OXeF$_2$][AsF$_6$] was warmed to −50 °C in aHF. The thermochemical cycle corresponding to eq 6 shows that

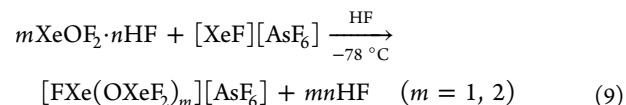this reaction is spontaneous at −78 °C ($\Delta G_{194.15}$ = −1485.5 kJ; Table 1).

The reaction of an equivalent amount of AsF$_5$ with [HOXe(F)$_2$OXeF$_2$][AsF$_6$] in aHF at −78 °C did not lead to [HOXeF$_2$][AsF$_6$] as expected, but promoted decomposition of [HOXe(F)$_2$OXeF$_2$][AsF$_6$] to [Xe$_2$F$_3$][AsF$_6$] (eq 7) ($\Delta G_{194.15}$ = −472.4 kJ mol$^{-1}$; Table 1). The anion likely plays a significant role in stabilizing the cation through ion-pair formation (vide infra). The additional AsF$_5$ molecule presumably bridges to the AsF$_6$$^-$ anion, rendering it less fluorobasic and less strongly ion paired, thereby promoting decomposition. In addition, the water formed during the synthesis of [HOXe(F)$_2$OXeF$_2$]-[AsF$_6$] (eq 5) also reacts with HF and AsF$_5$ to form [H$_3$O][AsF$_6$] (eq 8):

$$[HOXe(F)_2OXeF_2][AsF_6]_{(s)} \xrightarrow[-78\,°C]{HF/AsF_5} [Xe_2F_3][AsF_6]_{(s)}$$
$$+ O_{2(g)} + HF_{(l)} \quad (7)$$

$$HF + H_2O + AsF_5 \xrightarrow[-78\,°C]{HF} [H_3O][AsF_6] \quad (8)$$

In an effort to obtain a soluble salt of the HOXe(F)$_2$OXeF$_2$$^+$ cation, an attempt was made to synthesize the SbF$_6$$^-$ salt from [H$_3$O][SbF$_6$] by analogy with the synthesis of the AsF$_6$$^-$ salt (eq 5). Instead, the SbF$_6$$^-$ salt proved to be unstable, rapidly decomposing to [Xe$_3$OF$_3$][SbF$_6$] within several minutes when [H$_3$O][SbF$_6$] and XeOF$_2$·$n$HF were mixed in HF at −78 °C. This again suggests (vide supra) that AsF$_6$$^-$ plays a major role in stabilizing HOXe(F)$_2$OXeF$_2$$^+$ through the stronger ion pairing that results from its greater fluorobasicity relative to that of SbF$_6$$^-$.[9] The aforementioned reaction is similar to the previously reported reaction of XeF$_4$ with [H$_3$O][SbF$_6$] in HF.[18] Raman spectroscopy of the products in the later study indicated formation of [Xe$_3$OF$_3$][SbF$_6$], [XeF][SbF$_6$], and [Xe$_2$F$_3$][SbF$_6$] where HOXeF$_2$$^+$ was a postulated intermediate. The current study suggests that the more likely intermediate in this reaction is the HOXe(F)$_2$OXeF$_2$$^+$ cation.

*[FXe$^{II}$OXe$^{IV}$F$_2$][PnF$_6$] (Pn = As, Sb) and [FXe$^{II}$OXe$^{IV}$(F)$_2$OXe$^{IV}$F$_2$][AsF$_6$].* The significant basicity of oxygen in XeOF$_2$ and its propensity to protonate in strong acid media (vide supra), as well as the existence of several weak, unidentified peaks in the Raman spectrum of [HOXeF$_2$][AsF$_6$], led to attempts to synthesize an XeOF$_2$ adduct of XeF$^+$ containing a Xe$^{II}$−O−Xe$^{IV}$ bridge.

Both [FXeOXeF$_2$][AsF$_6$] and [FXeOXe(F)$_2$OXeF$_2$][AsF$_6$] were synthesized by the reaction of [XeF][AsF$_6$] with stoichiometric amounts of fully solvated XeOF$_2$·$n$HF suspended in aHF at −78 °C (eq 9):

$$mXeOF_2 \cdot nHF + [XeF][AsF_6] \xrightarrow[-78\,°C]{HF}$$
$$[FXe(OXeF_2)_m][AsF_6] + mnHF \quad (m = 1, 2) \quad (9)$$

Over the course of 5−10 min, the pale yellow solid turned bright yellow; however, reaction times of approximately 1 week and occasional agitation were required for complete reaction. The products were isolated by removal of HF under dynamic vacuum at −78 °C, leaving behind bright yellow powders. In instances where XeOF$_2$ was suspended in aHF for time periods that were insufficient to allow complete solvation, intermediate mixtures of XeOF$_2$·$n$HF, [XeF][AsF$_6$], [FXeOXeF$_2$], and [FXeOXe(F)$_2$OXeF$_2$][AsF$_6$] resulted that required reaction times of 1 month or more to go to completion (eq 9). It is

therefore important to fully solvate $XeOF_2$ in aHF to form $XeOF_2 \cdot nHF$[3] prior to its reaction with $[XeF][AsF_6]$. It was also shown that $[FXeOXeF_2][AsF_6]$ and $[FXeOXe(F)_2OXeF_2]$-$[AsF_6]$ may be interconverted when reacted with additional $XeOF_2 \cdot nHF$ and $[XeF][AsF_6]$, respectively (eq 9).

Several studies were carried out under the aforementioned conditions using 4:1, 2:1, 4:3, 1:1, and 1:2 molar ratios of $XeOF_2 \cdot nHF/[XeF][AsF_6]$ to determine if longer chain cations could be formed. When a 4:1 molar ratio was used, t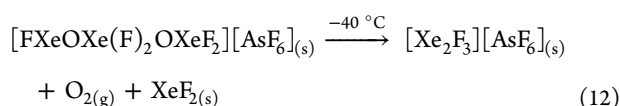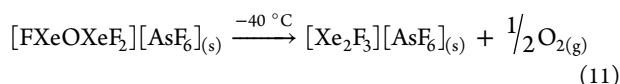he Raman spectrum only showed $[FXeOXe(F)_2OXeF_2][AsF_6]$ and unreacted $XeOF_2 \cdot nHF$. The 2:1 molar ratio only gave $[FXeOXe(F)_2OXeF_2][AsF_6]$ whereas the 4:3 molar ratio yielded a mixture of $[FXeOXe(F)_2OXeF_2][AsF_6]$ and $[FXeOXeF_2][AsF_6]$. The 1:1 and 1:2 molar ratios only yielded $[FXeOXeF_2][AsF_6]$, with unreacted $[XeF][AsF_6]$ also being present when a 1:2 molar ratio was used. The results indicate that no cations other than $[FXeOXeF_2][AsF_6]$ and $[FXeOXe(F)_2OXeF_2][AsF_6]$ were formed at −78 °C.
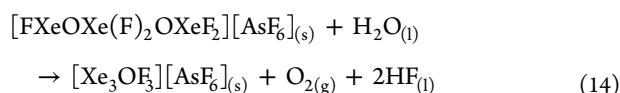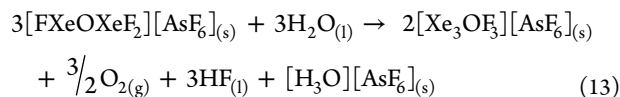
The mixed-oxidation state $FXeOXeF_2^+$ cation was also formed by the reaction of $XeOF_2 \cdot nHF$ with 0.5 equiv of $AsF_5$ in aHF solvent at −78 °C (eq 10). It is presumed that superacidic conditions promote $O_2$ elimination to give $FXeOXeF_2^+$:

$$2XeOF_2 \cdot nHF + AsF_5 \xrightarrow[-78\,°C]{HF/AsF_5} [FXeOXeF_2][AsF_6] + \tfrac{1}{2}O_2$$
$$+ 2nHF \qquad (10)$$

Both $[FXeOXeF_2][AsF_6]$ and $[FXeOXe(F)_2OXeF_2][AsF_6]$ were stable as precipitates under HF solvent and as dry powders for several weeks at −78 °C under anhydrous conditions, but began to decompose to $[Xe_2F_3][AsF_6]$ upon warming to −40 °C (eqs 11 and 12):

$$[FXeOXeF_2][AsF_6]_{(s)} \xrightarrow{-40\,°C} [Xe_2F_3][AsF_6]_{(s)} + \tfrac{1}{2}O_{2(g)}$$
$$(11)$$

$$[FXeOXe(F)_2OXeF_2][AsF_6]_{(s)} \xrightarrow{-40\,°C} [Xe_2F_3][AsF_6]_{(s)}$$
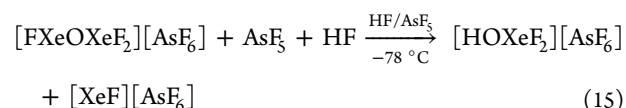$$+ O_{2(g)} + XeF_{2(s)} \qquad (12)$$

The main factor contributing to the spontaneities of both decomposition reactions ($\Delta G_{194.15} = -229.1$ and $-432.2$ kJ mol$^{-1}$, respectively; Table 1) is the reaction enthalpy (see Thermochemistry, Supporting Information). Sample storage for approximately 1 month at −78 °C resulted in sufficient water diffusion through the FEP reactor walls to hydrolyze both cations to $[Xe_3OF_3][AsF_6]$ (eq 13 and 14) as evidenced by the formation of deep red-orange crystals that were shown to be $[Xe_3OF_3][AsF_6]$ by Raman spectroscopy and crystallographic unit cell determinations:[18]

$$3[FXeOXeF_2][AsF_6]_{(s)} + 3H_2O_{(l)} \rightarrow 2[Xe_3OF_3][AsF_6]_{(s)}$$
$$+ \tfrac{3}{2}O_{2(g)} + 3HF_{(l)} + [H_3O][AsF_6]_{(s)} \qquad (13)$$

$$[FXeOXe(F)_2OXeF_2][AsF_6]_{(s)} + H_2O_{(l)}$$
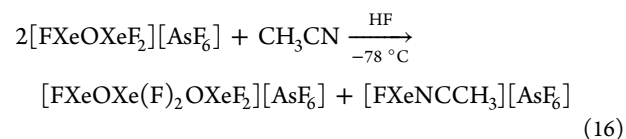$$\rightarrow [Xe_3OF_3][AsF_6]_{(s)} + O_{2(g)} + 2HF_{(l)} \qquad (14)$$

Both hydrolytic pathways are supported by thermochemical cycles that give negative $\Delta G_{194.15}$ values for both reactions (−745.4 and −491.4 kJ mol$^{-1}$, respectively; Table 1). Reaction of freshly prepared $[FXeOXeF_2][AsF_6]$ with 1 equiv of $AsF_5$ in

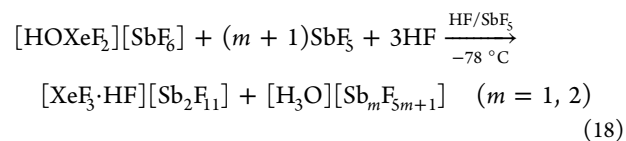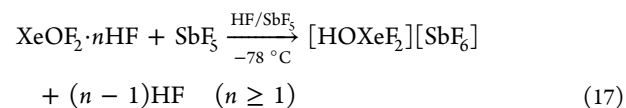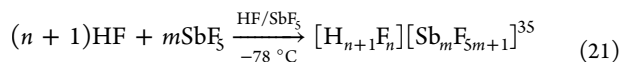aHF yielded a mixture of $[HOXeF_2][AsF_6]$ and $[XeF][AsF_6]$ (eq 15):

$$[FXeOXeF_2][AsF_6] + AsF_5 + HF \xrightarrow[-78\,°C]{HF/AsF_5} [HOXeF_2][AsF_6]$$
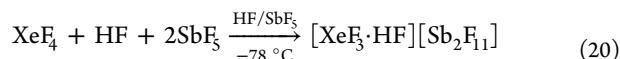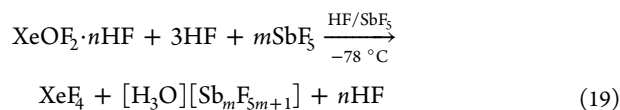$$+ [XeF][AsF_6] \qquad (15)$$

In further efforts to obtain soluble $FXeOXeF_2^+$ and $FXeOXe(F)_2OXeF_2^+$ salts, the syntheses of the $SbF_6^-$ salts were attempted by analogy with the $AsF_6^-$ salts (eq 9) using $[XeF][SbF_6]$. Both reactions proceeded more rapidly than those of their $AsF_6^-$ analogues, requiring only 24 h to go to completion; however, only $[FXeOXeF_2][SbF_6]$ formed, which had a more intense yellow color than $[FXeOXeF_2][AsF_6]$. When the synthesis of $[FXeOXe(F)_2OXeF_2][SbF_6]$ was attempted by analogy with eq 9, a mixture of $[FXeOXeF_2]$-$[SbF_6]$ and $XeOF_2 \cdot nHF$ was observed by Raman spectroscopy. No further reaction occurred even after the sample had been warmed to −50 °C for 2 h. These results indicate that the anion plays a significant role in cation stabilization. Like its $AsF_6^-$ analogue, $[FXeOXeF_2][SbF_6]$ also exhibited no discernible solubility in aHF and began to decompose to $[Xe_2F_3][SbF_6]$ when warmed to −40 °C.

In a further effort to solubilize a salt of $FXeOXeF_2^+$, the synthesis of $FXeOXe(F)_2NCCH_3^+$ was attempted in aHF in a manner similar to that used for the synthesis of $FXeNCCH_3^+$.[42] However, $CH_3CN$ displaced $XeOF_2$, which in turn, reacted with $FXeOXeF_2^+$ to form $[FXeOXe(F)_2OXeF_2][AsF_6]$ and $[FXeNCCH_3][AsF_6]$ (eq 16):

$$2[FXeOXeF_2][AsF_6] + CH_3CN \xrightarrow[-78\,°C]{HF}$$
$$[FXeOXe(F)_2OXeF_2][AsF_6] + [FXeNCCH_3][AsF_6]$$
$$(16)$$

*$[H_5F_4][SbF_6] \cdot 2[XeF_3 \cdot HF][Sb_2F_{11}]$ and $[XeF_3 \cdot HF][Sb_2F_{11}]$.* In yet another attempt to obtain a soluble $HOXeF_2^+$ salt suitable for crystal growth, the synthesis of the $SbF_6^-$ salt was attempted in the superacid medium, aHF/SbF$_5$. Because pure SbF$_5$ freezes at 7 °C[43] and is unsuitable for low-temperature reactions with $XeOF_2 \cdot nHF$, a freshly prepared aHF solution of SbF$_5$ (∼17 mol %) was decanted into a fluoroplastic reaction tube containing $XeOF_2 \cdot nHF$ under aHF at −196 °C, warmed to −78 °C, and thoroughly mixed. The sample was then warmed to −50 °C until all of the solid dissolved and then cooled to −78 °C. Over the course of 24 h, colorless crystals formed that were shown to be a mixture of $[H_5F_4][SbF_6] \cdot 2[XeF_3 \cdot HF][Sb_2F_{11}]$, $[XeF_3 \cdot HF][Sb_2F_{11}]$, and $[XeF_3][SbF_6]$ (see the X-ray Crystallography section). Under these superacidic conditions, the hydroxyl group of the cation was protonated and water was displaced, yielding $XeF_3^+$ and $H_3O^+$ (eqs 17, 18 or 19, 20), with the hydronium ion salt remaining in solution:

$$XeOF_2 \cdot nHF + SbF_5 \xrightarrow[-78\,°C]{HF/SbF_5} [HOXeF_2][SbF_6]$$
$$+ (n-1)HF \quad (n \geq 1) \qquad (17)$$

$$[HOXeF_2][SbF_6] + (m+1)SbF_5 + 3HF \xrightarrow[-78\,°C]{HF/SbF_5}$$
$$[XeF_3 \cdot HF][Sb_2F_{11}] + [H_3O][Sb_mF_{5m+1}] \quad (m = 1, 2)$$
$$(18)$$

$$\text{XeOF}_2 \cdot n\text{HF} + 3\text{HF} + m\text{SbF}_5 \xrightarrow[-78\,°C]{\text{HF/SbF}_5}$$

$$\text{XeF}_4 + [\text{H}_3\text{O}][\text{Sb}_m\text{F}_{5m+1}] + n\text{HF} \qquad (19)$$

$$\text{XeF}_4 + \text{HF} + 2\text{SbF}_5 \xrightarrow[-78\,°C]{\text{HF/SbF}_5} [\text{XeF}_3 \cdot \text{HF}][\text{Sb}_2\text{F}_{11}] \qquad (20)$$

$$(n+1)\text{HF} + m\text{SbF}_5 \xrightarrow[-78\,°C]{\text{HF/SbF}_5} [\text{H}_{n+1}\text{F}_n][\text{Sb}_m\text{F}_{5m+1}]^{35} \qquad (21)$$

The high acidity of this medium resulted in the $\text{Sb}_2\text{F}_{11}^-$ anion, which is not observed under dilute conditions in HF solution,[44] and its novel countercation, $\text{XeF}_3 \cdot \text{HF}^+$ (eqs 17–20). The previously unobserved acidium ion, $\text{H}_5\text{F}_4^+$, crystallized as the $\text{SbF}_6^-$ salt (eq 21, where $n = 4$, $m = 1$).

**X-ray Crystallography.** Summaries of the refinement results and other crystallographic information for $[\text{H}_5\text{F}_4]$-$[\text{SbF}_6] \cdot 2[\text{XeF}_3 \cdot \text{HF}][\text{Sb}_2\text{F}_{11}]$, $[\text{XeF}_3 \cdot \text{HF}][\text{Sb}_2\text{F}_{11}]$, and $[\text{XeF}_3]$-$[\text{SbF}_6]$ are provided in Table 2. All three $\text{XeF}_3^+$ salts were

**Table 2. Summary of Crystal Data and Refinement Results for $[\text{H}_5\text{F}_4][\text{SbF}_6] \cdot 2[\text{XeF}_3 \cdot \text{HF}][\text{Sb}_2\text{F}_{11}]$, $[\text{XeF}_3 \cdot \text{HF}][\text{Sb}_2\text{F}_{11}]$, and $\beta$-$[\text{XeF}_3][\text{SbF}_6]$**

| | $[\text{H}_5\text{F}_4][\text{SbF}_6] \cdot$ $2[\text{XeF}_3 \cdot \text{HF}][\text{Sb}_2\text{F}_{11}]$ | $[\text{XeF}_3 \cdot \text{HF}]$ $[\text{Sb}_2\text{F}_{11}]$ | $\beta$-$[\text{XeF}_3]$ $[\text{SbF}_6]$ |
|---|---|---|---|
| space group | $P\bar{1}$ (no. 2) | $C/2c$ (no. 15) | $P2_1/c$ (no. 14) |
| $a$ (Å) | 7.5604(8) | 13.4120(4) | 5.2330(2) |
| $b$ (Å) | 8.4967(9) | 8.4709(4) | 15.6029(4) |
| $c$ (Å) | 13.017(1) | 10.4543(4) | 9.0388(2) |
| $\alpha$ (deg) | 85.469(4) | 90 | 90 |
| $\beta$ (deg) | 78.082(3) | 110.493(2) | 111.534(1) |
| $\gamma$ (deg) | 66.350(3) | 90 | 90 |
| $V$ (Å³) | 749.44(14) | 1112.56(8) | 686.51(5) |
| $Z$ (molecules/unit cell) | 2 | 4 | 4 |
| $M$ (g mol⁻¹) | 977.60 | 660.81 | 424.05 |
| $\rho_{calcd}$ (g cm⁻³) | 4.332 | 3.945 | 4.103 |
| $T$ (°C) | −173 | −173 | −173 |
| $\mu$ (mm⁻¹) | 7.87 | 8.04 | 8.99 |
| $\lambda$ (Å) | 0.71073 | 0.71073 | 0.71073 |
| $R_1{}^a$ | 0.0389 | 0.0251 | 0.0262 |
| $wR_2{}^b$ | 0.1011 | 0.0582 | 0.0613 |

$^a R_1 = \Sigma ||F_o| - |F_c|| / \Sigma |F_o|$ for $I > 2\sigma(I)$. $^b wR_2$ is defined as $\{\Sigma[w(F_o^2 - F_c^2)^2] / \Sigma w(F_o^2)^2\}^{1/2}$ for $I > 2\sigma(I)$.

isolated from HF/SbF$_5$ solutions of XeOF$_2 \cdot n$HF. Their bond lengths, bond angles, and contact distances are listed in Tables 3 and S2 (Supporting Information). Although the crystal structure of $\beta$-$[\text{XeF}_3][\text{SbF}_6]$ had been previously reported,[15] the present low-temperature (−173 °C) structure was determined at a higher precision and has been included in the Supporting Information to provide a better comparison with the structural parameters of $\text{XeF}_3^+ \cdot \text{HF}$ in the present study.

*$[H_5F_4][SbF_6] \cdot 2[XeF_3 \cdot HF][Sb_2F_{11}]$.* The crystal packing (Figure S1, Supporting Information) shows two adjacent and parallel planes containing $[\text{XeF}_3 \cdot \text{HF}][\text{Sb}_2\text{F}_{11}]$ units that alternate with a plane containing $[\text{H}_5\text{F}_4][\text{SbF}_6]$ units. All planes are parallel to the $a,b$-plane of the crystallographic unit cell.

Unlike $\text{H}_7\text{F}_6^+$,[35] the hydrogen atom positions of $\text{H}_5\text{F}_4^+$ in $[\text{H}_5\text{F}_4][\text{SbF}_6] \cdot 2[\text{XeF}_3 \cdot \text{HF}][\text{Sb}_2\text{F}_{11}]$ could not be located in the difference map, which was also the case for $\text{H}_3\text{F}_2^+$ and $\text{H}_2\text{F}^+$.[36]

The $\text{SbF}_6^-$ anion and fluorine atoms of the $\text{H}_5\text{F}_4^+$ cation form a chain structure (Figure 1) that is similar to those of $[\text{H}_2\text{F}][\text{Sb}_2\text{F}_{11}]$,[36] $[\text{H}_3\text{F}_2][\text{Sb}_2\text{F}_{11}]$,[35] and $[\text{H}_7\text{F}_6][\text{SbF}_6]$.[35] The shortest F---F distance between the $\text{SbF}_6^-$ anion and the $\text{H}_5\text{F}_4^+$ cation occurs for F(6)---F(19) (2.444(4) Å). Within the $\text{H}_5\text{F}_4^+$ cation, the shortest F---F distance occurs for the central pair of fluorine atoms (F(20)---F(20A), 2.293(5) Å). The F---F distance of the terminal fluorine atom pair (F(19)---F(20A), 2.337(3) Å), is longer than that of F(20)---F(20A). These distances are in good agreement with the F---F distances in $\text{H}_7\text{F}_6^+$ (2.284(4)−2.450(2) Å),[35] $\text{H}_3\text{F}_2^+$ (2.30(1)−2.41(1) Å),[36] and $\text{H}_2\text{F}^+$ (2.64−2.78 Å)[36] and exhibit the same F---F distance trends.

*$[XeF_3 \cdot HF][Sb_2F_{11}]$.* The $[\text{XeF}_3 \cdot \text{HF}][\text{Sb}_2\text{F}_{11}]$ salt was also isolated in the absence of $[\text{H}_5\text{F}_4][\text{SbF}_6]$. The crystal packing consists of alternating planes of $\text{XeF}_3 \cdot \text{HF}^+$ cations and $\text{Sb}_2\text{F}_{11}^-$ anions that are parallel to the $b,c$-plane (Figure S2, Supporting Information).

In the crystal structure of $[\text{XeF}_3 \cdot \text{HF}][\text{Sb}_2\text{F}_{11}]$, there is a 2-fold positional disorder about the diagonal that bisects the F(1)−Xe−F(2) angle of $\text{XeF}_3 \cdot \text{HF}$ so that the equatorial fluorine atom (F(1)) and one of the axial fluorine atoms (F(2)) are indistinguishable and the remaining axial fluorine atom (F(3)) cannot be distinguished from the fluorine atom (F(10)) of the coordinated HF molecule (Table 3 and Figure 2).

The secondary coordination spheres of xenon are very similar in $[\text{XeF}_3 \cdot \text{HF}][\text{Sb}_2\text{F}_{11}]$ and $[\text{H}_5\text{F}_4][\text{SbF}_6] \cdot 2[\text{XeF}_3 \cdot \text{HF}]$-$[\text{Sb}_2\text{F}_{11}]$ (Figure 3), with the long Xe---F contacts ranging from 2.935(1) to 2.967(1) Å and from 2.847(3) to 3.088(3) Å, respectively. There is an additional contact (Xe---F, 3.088(3) Å) in the $[\text{H}_5\text{F}_4][\text{SbF}_6] \cdot 2[\text{XeF}_3 \cdot \text{HF}][\text{Sb}_2\text{F}_{11}]$ crystal structure that occurs between the $\text{XeF}_3^+$ cation and the $\text{SbF}_6^-$ anion of $[\text{H}_5\text{F}_4][\text{SbF}_6]$, which presumably better anchors the cation to give an ordered structure.

*$XeF_3^+ \cdot HF$ in $[H_5F_4][SbF_6] \cdot 2[XeF_3 \cdot HF][Sb_2F_{11}]$ and $[XeF_3 \cdot HF]$-$[Sb_2F_{11}]$.* The "$\text{XeF}_3^+ \cdot \text{HF}$" cation is best described as an HF adduct of the $\text{XeF}_3^+$ cation, $\text{F}_3\text{Xe}---\text{FH}^+$, rather than as a protonated $\text{XeF}_4$ molecule. This description is based on similarities between the geometric parameters of $\text{XeF}_3^+$ in $\text{XeF}_3^+ \cdot \text{HF}$ and those of $\text{XeF}_3^+$ in $[\text{XeF}_3][\text{SbF}_6]$ (Figure 2) and $[\text{XeF}_3][\text{Sb}_2\text{F}_{11}]$,[8,14] as demonstrated in the ensuing discussion.

The Xe−F$_{eq}$ bond length (1.838(2) Å) of $[\text{H}_5\text{F}_4][\text{SbF}_6] \cdot 2[\text{XeF}_3 \cdot \text{HF}][\text{Sb}_2\text{F}_{11}]$ is equal to that of $[\text{XeF}_3][\text{SbF}_6]$ (1.840(2) Å) but is significantly shorter than the Xe−F bonds of $\text{XeF}_4$ (1.951(2), 1.954(2) Å).[45] The Xe−F$_{ax}$ bond lengths (1.880(2) and 1.890(2) Å) are also very similar to those of the $\text{SbF}_6^-$ salt (1.893(2) and 1.901(2) Å) and are significantly shorter than those in $\text{XeF}_4$. In contrast with other $\text{XeF}_3^+$ salts, which fluorine bridge to their respective anions,[8,12−15] the $\text{XeF}_3^+$ cation of $[\text{H}_5\text{F}_4][\text{SbF}_6] \cdot 2[\text{XeF}_3 \cdot \text{HF}][\text{Sb}_2\text{F}_{11}]$ has a short secondary contact (2.462(2) Å) to a HF molecule that lies in the $\text{XeF}_3^+$ plane and is best formulated as $\text{F}_3\text{Xe}---\text{FH}^+$. This contact is similar to the short secondary contact that occurs between the cation and anion of $[\text{XeF}_3][\text{SbF}_6]$ (2.485(1) Å). The F$_{eq}$−Xe−F$_{ax}$ (81.4(1)°, 81.0(1)°), F$_{ax}$−Xe−F$_{ax}$ (162.3(1)°), and F$_{ax}$−Xe---F$_F$ (78.8(1)°, 118.77(9)°) bond angles of $\text{XeF}_3^+ \cdot \text{HF}$ are also very similar to those of $[\text{XeF}_3][\text{SbF}_6]$ (F$_{eq}$−Xe−F$_{ax}$, 79.72(8)°, 79.74(7)°; F$_{ax}$−Xe−F$_{ax}$, 159.45(8)°; F$_{ax}$−Xe---F$_{Sb}$, 73.06(6)°, 127.47(6)°).

The positionally averaged Xe−F$_{ax}$/Xe−F$_{eq}$ and Xe−F$_{ax}$/Xe−F$_H$ bond lengths of $[\text{XeF}_3 \cdot \text{HF}][\text{Sb}_2\text{F}_{11}]$ are 1.865(1) and 2.186(1) Å, respectively, and are in good agreement with the

**Table 3. Experimental and Calculated Bond Lengths (Å) and Bond Angles (deg) for XeF$_3^+$·HF**

| | XeF$_3^+$·HF | | | | |
| --- | --- | --- | --- | --- | --- |
| | exptl | | calcd[a] | | |
| | [H$_5$F$_4$][SbF$_6$]·2[XeF$_3$·HF][Sb$_2$F$_{11}$] | [XeF$_3$·HF][Sb$_2$F$_{11}$][b] | B3LYP | PBE1PBE | MP2 |
| Xe(1)−F(1) | 1.880(2) | 1.865(1) | 1.916 | 1.894 | 1.892 |
| Xe(1)−F(2) | 1.838(2) | 1.865(1) | 1.870 | 1.847 | 1.839 |
| Xe(1)−F(3) | 1.890(2) | 2.186(2) | 1.916 | 1.894 | 1.892 |
| Xe(1)---F(10) | 2.462(2) | 2.186(2) | 2.556 | 2.537 | 2.550 |
| F(10)−H | | | 0.937 | 0.933 | 0.934 |
| F(1)−Xe(1)−F(2) | 81.4(1) | 81.40(8) | 84.7 | 84.1 | 83.7 |
| F(1)−Xe(1)−F(3) | 162.3(1) | 161.12(6) | 169.3 | 168.3 | 167.4 |
| F(1)−Xe(1)---F(10) | 78.8(1) | 79.72(6) | 95.3 | 95.8 | 96.3 |
| F(2)−Xe(1)−F(3) | 81.0(1) | 79.72(6) | 84.7 | 84.1 | 83.7 |
| F(2)−Xe(1)---F(10) | 160.2(1) | 161.12(6) | 176.7 | 176.8 | 177.1 |
| F(3)−Xe(1)---F(10) | 118.77(9) | 119.15(9) | 95.4 | 95.9 | 96.3 |
| Xe(1)---F(10)−H | | | 141.9 | 141.9 | 152.8 |

[a]The aug-cc-pVTZ(-PP) basis set was used. [b]The F(1)/F(2) and F(3)/F(10) positions are disordered.
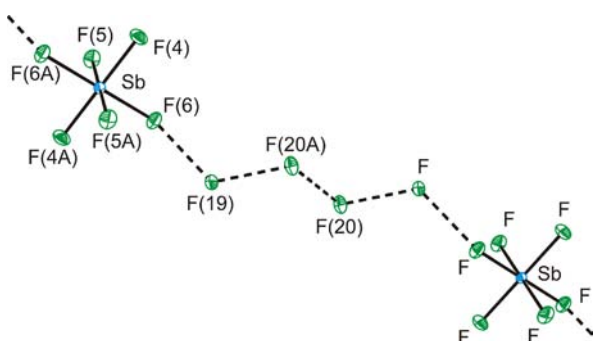


**Figure 1.** [H$_5$F$_4$][SbF$_6$] unit in the X-ray crystal structure of [H$_5$F$_4$][SbF$_6$]·2[XeF$_3$·HF][Sb$_2$F$_{11}$]. Thermal ellipsoids are shown at the 30% probability level. The hydrogen atoms of H$_5$F$_4^+$ could not be observed in the difference map.

averages of the corresponding bond lengths in [H$_5$F$_4$][SbF$_6$]·2[XeF$_3$·HF][Sb$_2$F$_{11}$], 1.859(3) and 2.176(3) Å, respectively.

**Raman Spectroscopy.** The low-temperature Raman spectra of solid [$^{1/2}$H$^{16/18}$OXeF$_2$][AsF$_6$], [H$^{16/18}$OXe(F)$_2$$^{16/18}$OXeF$_2$][AsF$_6$], [FXe$^{16/18}$OXeF$_2$][AsF$_6$], and [FXe$^{16/18}$OXe(F)$_2$$^{16/18}$OXeF$_2$][AsF$_6$] were identical to the low-temperature spectra of their precipitates recorded under solid HF solvent (see Syntheses, Properties, and Reactivities), with the latter providing better signal-to-noise ratios. Consequently, the Raman spectra (Figures 4−7) and their assignments (Tables 4−7 and S3−S7, Supporting Information) are for spectra recorded under solid HF. Relevant NBO valencies, bond orders, and NPA charges are provided in Table S9 (Supporting Information) and are discussed in the [FXe$^{II}$OXe$^{IV}$F$_2$][PnF$_6$] (Pn = As, Sb) section below.

The spectral assignments were made by comparison with the calculated frequencies and Raman intensities (Tables 4−7) of the energy-minimized geometries of the gas-phase cations (Figure 8), with the exception of $^{1/2}$H$^{16/18}$OXeF$_2^+$, which was also calculated for the [$^{1/2}$H$^{16/18}$OXeF$_2$][AsF$_6$] ion pair (Figure 8c). Vibrational frequencies calculated at the PBE1PBE, B3LYP, and MP2 levels of theory (Tables S3−S7, Supporting Information) reproduced the observed frequency trends across the series of compounds; only the PBE1PBE values are referred to in the ensuing discussion. As observed for Xe$_3$OF$_3^+$,[18] the calculated Raman intensities of the Xe−O stretching bands are consistently overestimated for each system when compared

with the experimental intensities. In all cases, symmetry lowering is expected to split the two Raman-active degenerate modes of octahedral AsF$_6^-$, $\nu_2$(E$_g$) and $\nu_5$(T$_{2g}$). Additional vibrational band splittings, such as for the $\nu_1$(A$_{1g}$) band, do not result from site symmetry lowering and are likely attributable to vibrational coupling within the unit cell (factor-group splitting); however, in the absence of crystal structures, factor-group analyses could not be performed. Consequently, the anion bands were assigned by comparison with other AsF$_6^-$ salts in which there are significant ion-pair interactions by means of fluorine bridging between their cations and the anions.[46−48] In those cases where split bands are observed in the cation spectrum, the splittings are likely attributable to factor-group splitting and are referred to within the ensuing discussion as "splittings" or "split bands".

*[HOXeF$_2$][AsF$_6$].* The Raman spectra of the $^{1/2}$H$^{16/18}$OXeF$_2^+$ cation exhibit two bands that are $^{1/2}$H-dependent and four bands that are both $^{1/2}$H- and $^{16/18}$O-dependent, in good agreement with the calculated spectra where one band is predicted to be $^{1/2}$H-dependent and five bands are both $^{1/2}$H- and $^{16/18}$O-dependent. The minor differences that arise between the experimental and calculated frequencies of modes involving the hydrogen atom likely result because the calculated ion-pair models are for isolated gas-phase ion pairs (see the Computational Results section). It is anticipated that there will be significant hydrogen bonding among nearest-neighbor ion pairs in the solid state.

The most intense cation bands occur at 543.6 and 554.7 cm$^{-1}$ in the Raman spectrum and do not show isotopic shifts. These split bands are assigned to the symmetric axial XeF$_2$ stretching mode, $\nu$(Xe$_1$F$_1$) + $\nu$(Xe$_1$F$_2$), which is in good agreement with the calculated value (562.8 cm$^{-1}$), and with the symmetric axial XeF$_2$ stretching modes in $\alpha$- and $\beta$-[XeF$_3$]-[SbF$_6$] ($\alpha$, 573; $\beta$, 564 and 576 cm$^{-1}$).[9] The out-of-phase $\nu$(Xe$_1$F$_1$) − $\nu$(Xe$_1$F$_2$) stretching mode of HOXeF$_2^+$ is assigned to a weak band at 602.0 cm$^{-1}$ and is in good agreement with the calculated value (618.9 cm$^{-1}$) and with the asymmetric axial XeF$_2$ stretching mode in $\alpha$- and $\beta$-[XeF$_3$][SbF$_6$] ($\alpha$, 609; $\beta$, 604 cm$^{-1}$).[9] The largest $^{16/18}$O-isotopic shift (−30.9 cm$^{-1}$) occurs for the band at 646.7 cm$^{-1}$. This band also shows a $^{1/2}$H-isotopic shift (−5.8 cm$^{-1}$) and is assigned to $\nu$(Xe$_1$O$_1$), with calculated $^{1/2}$H- and $^{16/18}$O-isotopic shifts of −6.8 and −27.6 cm$^{-1}$, respectively. The in-plane bend, $\delta$(OXe$_1$F$_1$) −
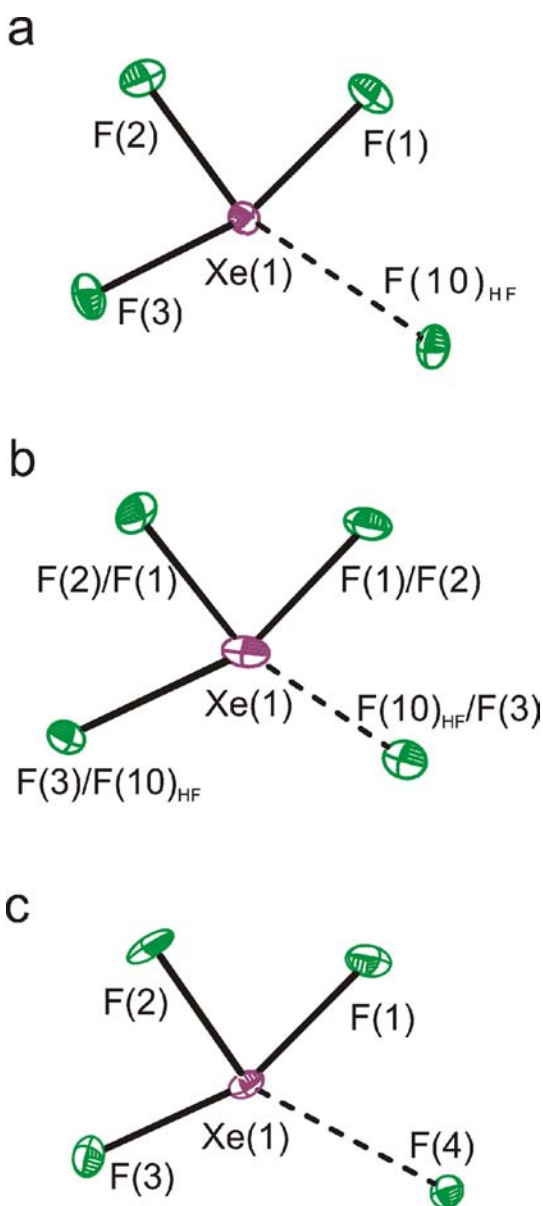
**Figure 2.** XeF$_3^+$ cations in the X-ray crystal structures of (a) [H$_5$F$_4$][SbF$_6$]·2[XeF$_3$·HF][Sb$_2$F$_{11}$], (b) [XeF$_3$·HF][Sb$_2$F$_{11}$], and (c) [XeF$_3$][SbF$_6$]. Thermal ellipsoids are shown at the 50% probability level.



**Figure 3.** Primary and secondary coordination spheres of XeF$_3^+$·HF in the X-ray crystal structures of (a) [H$_5$F$_4$][SbF$_6$]·2[XeF$_3$·HF][Sb$_2$F$_{11}$] and (b) [XeF$_3$·HF][Sb$_2$F$_{11}$]. Thermal ellipsoids are shown at the 50% probability level.

$\delta$(OXe$_1$F$_2$), predicted at 298.0 cm$^{-1}$ ($^{16/18}\Delta\nu$, −10.3 cm$^{-1}$), is assigned to the Raman band observed at 307.0 cm$^{-1}$ ($^{16/18}\Delta\nu$, −10.1 cm$^{-1}$). The broad band at 194.6 cm$^{-1}$ also shows $^{1/2}$H and $^{16/18}$O sensitivities (−7.0 and −8.2 cm$^{-1}$, respectively) and is assigned to $\rho_r$(HOXe$_1$F$_1$F$_2$)$_{o.o.p.}$ (calcd, 117.7 cm$^{-1}$; −3.0 and −3.3 cm$^{-1}$, respectively). The discrepancies between the experimental and calculated vibrational frequency and isotopic shifts may result from hydrogen bonding involving neighboring ion pairs.

The highest frequency band expected for HOXeF$_2^+$, $\nu$(O$_1$H), is predicted to occur at 3763.9 cm$^{-1}$ and to show significant $^{1/2}$H and $^{16/18}$O sensitivities (−1023 and −12.5 cm$^{-1}$, respectively). Presumably, this mode could not be observed in the Raman spectrum, because $\nu$(OH) bands are often broad and weak due to the small polarizability changes associated with O−H stretches. The respective XeOH bending and wagging modes are assigned to weak bands at 1264.6 and 328.0 cm$^{-1}$

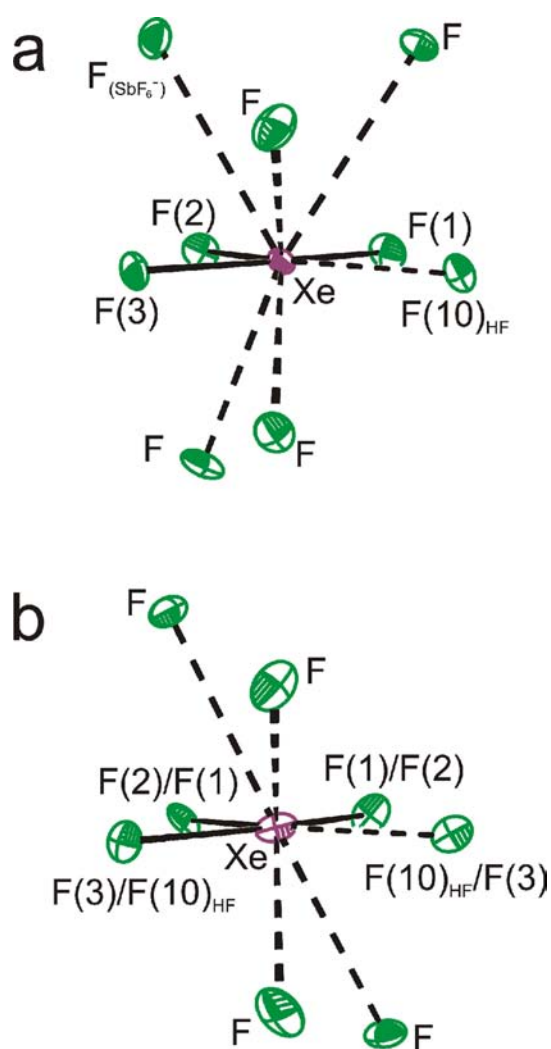(broad) that display $^{1/2}$H-isotopic shifts of −337.0 and −67.2 cm$^{-1}$, respectively, with the bending mode also displaying a $^{16/18}$O-isotopic shift of −3.4 cm$^{-1}$. Although the isotopic shifts are well modeled by the calculations [$^{1/2}\Delta\nu$, −306.2 and −61.5 cm$^{-1}$; $^{16/18}\Delta\nu$, −3.3 cm$^{-1}$], the XeOH wagging frequency is underestimated (calcd, 223.2 cm$^{-1}$) likely because the simplified model neglects hydrogen-bonding interactions involving neighboring ion pairs in the solid state which are expected to shift this mode to higher frequency.[49]

The in-plane and out-of-plane XeF$_2$ bending modes occur at 210.4 and 235.6 cm$^{-1}$, respectively, and display neither $^{1/2}$H- nor $^{16/18}$O-isotopic shifts, in agreement with the calculated ion-pair frequencies.

*[FXe$^{II}$OXe$^{IV}$F$_2$][PnF$_6$] (Pn = As, Sb).* With the exception of the anion modes, the Raman spectra of [FXe$^{16}$OXeF$_2$][AsF$_6$] and [FXe$^{16}$OXeF$_2$][SbF$_6$] are nearly identical, and the spectra of [FXe$^{16/18}$OXeF$_2$][AsF$_6$] closely resemble those of [H$^{16/18}$OXeF$_2$][AsF$_6$].

Although the calculated Xe$^{II}$−O$_1$ bond of FXeOXeF$_2^+$ is 0.40 Å longer than the Xe$^{IV}$−O$_1$ bond (see calculated geometries, Figure 8), the $\nu$($^{IV}$Xe$_1$O$_1$) and $\nu$($^{II}$Xe$_2$O$_1$) stretches are strongly coupled and give rise to $\nu$($^{IV}$Xe$_1$O$_1$) − $\nu$($^{II}$Xe$_2$O$_1$) and

**Figure 4.** Raman spectra of natural abundance (lower trace) and 97.8% $^{18}$O-enriched (upper trace) $[HOXeF_2][AsF_6]$ recorded at −150 °C under HF solvent using 1064-nm excitation. Symbols denote FEP sample tube lines (*), an instrumental artifact (†), and $[XeF][AsF_6]$ impurity (‡).
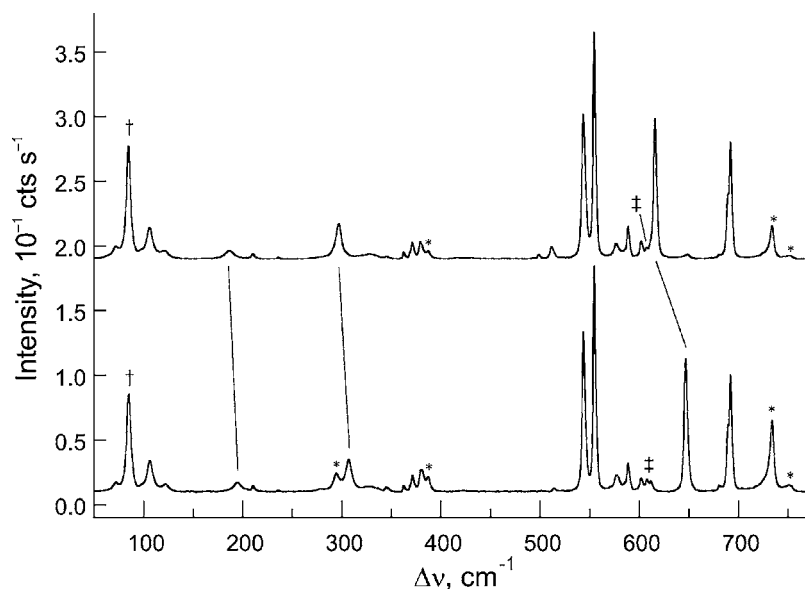


**Figure 5.** Raman spectra of natural abundance (lower trace) and 97.8% $^{18}$O-enriched (upper trace) $[FXeOXeF_2][AsF_6]$ recorded at −150 °C under HF solvent using 1064-nm excitation. Symbols denote $[FXe^{18}OXe(F)_2{}^{18}OXe(F)_2][AsF_6]$ impurity (‡), FEP sample tube lines (*), and an instrumental artifact (†).

$\nu(^{IV}Xe_1O_1) + \nu(^{II}Xe_2O_1)$, which occur at very different frequencies. The out-of-phase stretching mode is at 645.4 cm$^{-1}$ ($^{16/18}\Delta\nu$, −29.8 cm$^{-1}$) and is in good agreement with the calculated values (679.1 cm$^{-1}$; $^{16/18}\Delta\nu$, −31.3 cm$^{-1}$), whereas the split in-phase stretching mode occurs at 405.1 and 409.4 cm$^{-1}$ ($^{16/18}\Delta\nu$, −21.1, −19.1 cm$^{-1}$, respectively). The calculated frequency and isotopic shift (342.5 cm$^{-1}$; $^{16/18}\Delta\nu$, −16.5 cm$^{-1}$) are likely underestimated because the gas-phase model does not take ion pairing into account.

The only other band displaying a $^{16/18}$O-isotopic shift (−10.6 cm$^{-1}$) occurs at 300.6 cm$^{-1}$ and is assigned to $\delta(O^{IV}Xe_1F_1) - \delta(O^{IV}Xe_1F_2)$. Both values agree well with the calculated frequency and isotopic shift (298.2 cm$^{-1}$; $^{16/18}\Delta\nu$, −11.7 cm$^{-1}$) and with the corresponding band in $[HOXeF_2][AsF_6]$ (307.0 cm$^{-1}$; $^{16/18}\Delta\nu$, −10.1 cm$^{-1}$).

The split band at 545.6, 556.0 cm$^{-1}$ is assigned to the terminal $\nu(^{II}Xe_2F_3)$ stretching mode that occurs at significantly lower frequency than $\nu(XeF)$ in $[XeF][AsF_6]$ (607 and 611 cm$^{-1}$).[8] The lower $^{II}Xe_2$–$F_3$ stretching frequency indicates
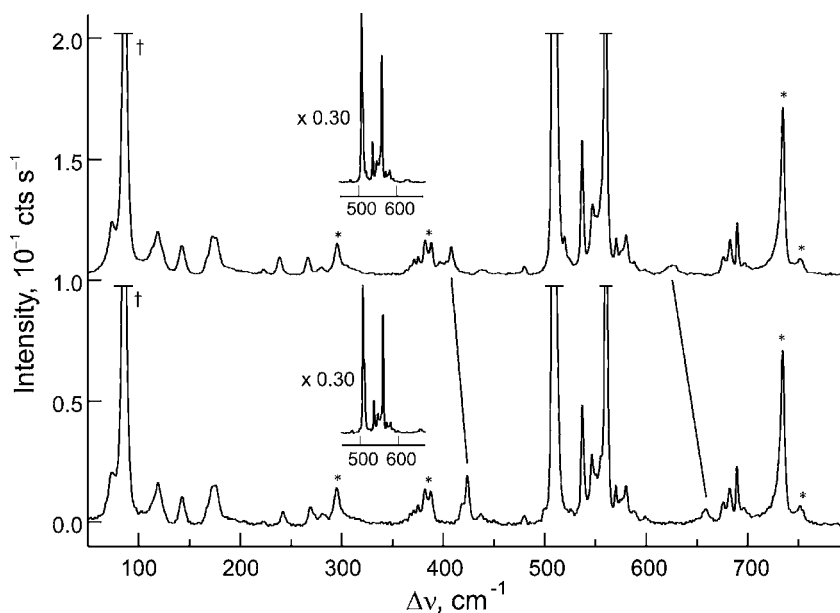
**Figure 6.** Raman spectra of natural abundance (lower trace) and 97.8% ^{18}O-enriched (upper trace) $[HOXe(F)_2OXe(F)_2][AsF_6]$ recorded at −150 °C under HF solvent using 1064-nm excitation. Symbols denote FEP sample tube lines (*) and an instrumental artifact (†).
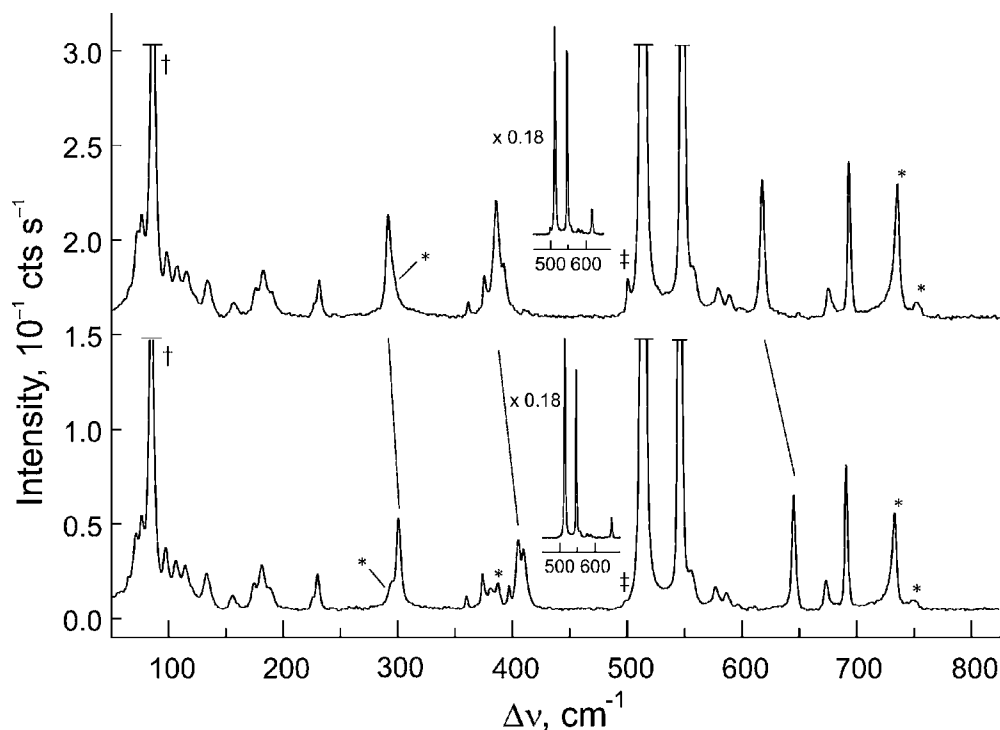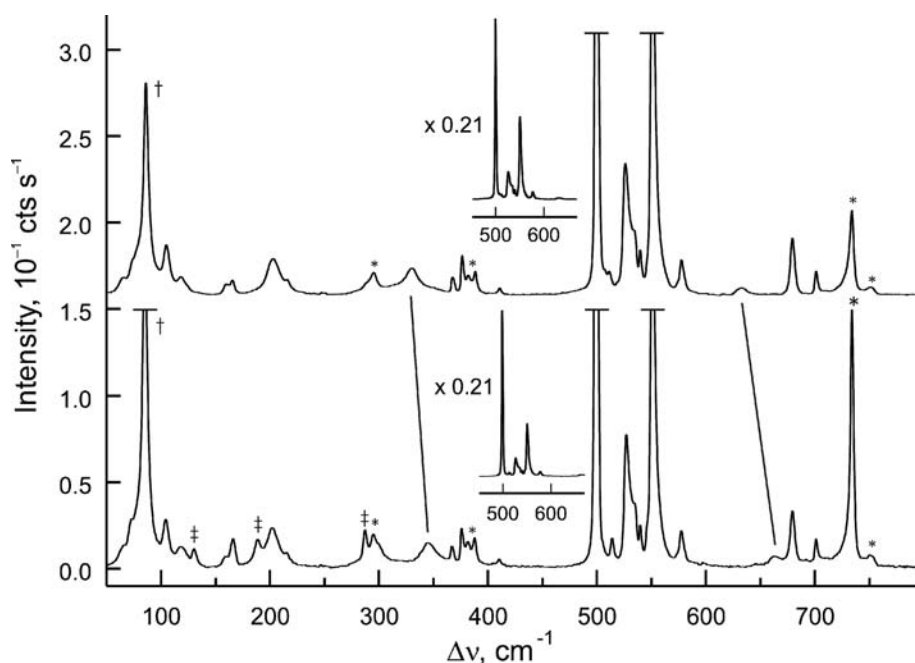


**Figure 7.** Raman spectra of natural abundance (lower trace) and 97.8% ^{18}O-enriched (upper trace) $[FXeOXe(F)_2OXe(F)_2][AsF_6]$ recorded at −150 °C under HF solvent using 1064-nm excitation. Symbols denote $XeOF_2 \cdot nHF$ (‡) impurity, FEP sample tube lines (*), and an instrumental artifact (†).

significant covalent bonding between $O_1$ and [II]$Xe_2$ (b.o., 0.23) that renders [II]$Xe_2$ less positive (charge, 1.24) than xenon in $XeF^+$ (charge, 1.33) (Table S9, Supporting Information). Charge transfer is also reflected in the relative [II]$Xe_2$−$F_3$ (0.34) and $XeF^+$ (0.48) bond orders.

The $\nu$([IV]$Xe_1F_1$) + $\nu$([IV]$Xe_1F_2$) stretch of $FXeOXeF_2^+$ occurs at lower frequency (513.5 cm$^{-1}$) than that of $HOXeF_2^+$ (543.6, 554.7 cm$^{-1}$) but at higher frequency than that of $XeOF_2$ (467 cm$^{-1}$),[3] which is consistent with cation formation and decreases in the $Xe^{IV}$−O bond orders and increases in the $Xe^{IV}$−F bond orders upon coordination: $Xe^{IV}$ charges [$FXe^{II}OXe^{IV}F_2^+$, 2.14; $HOXeF_2^+$, 2.18; $XeOF_2$, 2.02] and bond orders [$Xe^{IV}$−O:

$XeOF_2$, 0.79; $FXe^{II}OXe^{IV}F_2^+$, 0.72; $HOXeF_2^+$, 0.60; and $Xe^{IV}$−F: $XeOF_2$, 0.35; $FXe^{II}OXe^{IV}F_2^+$, 0.40; $HOXeF_2^+$, 0.43]. The $\nu$([IV]$Xe_1F_1$) − $\nu$([IV]$Xe_1F_2$) symmetric stretch was too weak to be observed (cf. calculated intensity, Table S5, Supporting Information).

The in-plane and out-of-plane $F_1$−[IV]$Xe_1$−$F_2$ bending modes occur as split bands at 181.3, 187.7 and 225.6, 229.9 cm$^{-1}$, respectively. The experimental frequencies of both modes are also in good agreement with their calculated values (180.7, 183.0 and 208.2, 228.3 cm$^{-1}$).

$[HOXe^{IV}(F)_2OXe^{IV}F_2][AsF_6]$ and $[FXe^{II}OXe^{IV}(F)_2OXe^{IV}F_2]$-$[AsF_6]$. Correlations among the experimental frequencies and

**Table 4. Experimental Raman Frequencies[a] and Intensities[b] for $[^{1/2}H^{16/18}OXeF_2][AsF_6]^c$**

| $^1H^{16}O$ | $^1H^{18}O$ | $^{16/18}\Delta\nu$ | $^2H^{16}O$ | $^2H^{18}O$ | $^{16/18}\Delta\nu$ | $^{1(16)/2(16)}\Delta\nu$ | $^{1(18)/2(18)}\Delta\nu$ | assignment[d] |
|---|---|---|---|---|---|---|---|---|
| n.o. | n.o. | n.o. | n.o. | n.o. | n.o. | n.o. | n.o. | $\nu(O_1H)$ |
| 1264.6(2) | 1261.2(2) | −3.4 | 927.6(1) | 922.0(1) | −5.6 | −337.0 | −339.2 | $\delta(Xe_1O_1H)$ |
| 692.0(52) | 692.0(52) | 0.0 | 692.0(66) | 691.9(55) | 0.1 | 0.0 | −0.1 | } $\nu_1(A_{1g})(AsF_6^-)$ |
| 689.7(30) | 689.6(29) | −0.1 | 689.2(32) | 689.1(31) | −0.1 | −0.5 | −0.5 | |
| 646.7(59) | 615.8(62) | −30.9 | 640.9(66) | 611.0(68)[f] | −29.9 | −5.8 | −4.8 | $\nu(Xe_1O_1)$ |
| 602.0(6) | 601.9(8) | −0.1 | 600.5(7) | 600.3(9) | −0.2 | −1.5 | −1.6 | $\nu(Xe_1F_1) - \nu(Xe_1F_2)$ |
| 588.8(12) | 588.4(14) | −0.4 | 588.1(16) | 587.8(18) | −0.3 | −0.7 | −0.6 | } $\nu_2(E_g)(AsF_6^-)$ |
| 577.0(7) | 576.3(7) | −0.7 | 567.8(7) | 567.1(9) | −0.7 | −9.2 | −9.2 | |
| 554.7(100) | 554.6(100) | −0.1 | 554.6(100) | 554.5(100) | −0.1 | −0.1 | −0.1 | } $\nu(Xe_1F_1) + \nu(Xe_1F_2)$ |
| 543.6(71) | 543.5(64) | −0.1 | 543.5(66) | 543.1(62) | −0.4 | −0.1 | −0.4 | |
| 380.2(4)[e] | 379.2(6)[e] | −1.0 | 379.2(4) | 378.9(6) | −0.3 | −1.0 | −0.3 | } $\nu_5(T_{2g})(AsF_6^-)$ |
| 371.6(7) | 371.0(7) | −0.6 | 371.1(7) | 370.7(9) | −0.4 | −0.5 | −0.3 | |
| 362.3(3) | 362.3(3) | 0.0 | 362.4(3) | 362.2(4) | −0.2 | 0.1 | −0.1 | |
| 328.0(2),br | 327.5(2),br | −0.5 | 260.8(3),br | 259.2(3),br | −1.6 | −67.2 | −68.3 | $\rho_w(Xe_1O_1H)$ |
| 307.0(14) | 296.9(13) | −10.1 | 313.1(9) | 301.9(9) | −11.2 | 6.1 | 5.0 | $\delta(OXe_1F_1) - \delta(OXe_1F_2)$ |
| 235.6(1) | 236.1(1) | 0.5 | 235.5(1) | 236.2(1) | 0.7 | 0.1 | 0.1 | $\delta(F_1Xe_1F_2)_{o.o.p.}$ |
| 210.4(2) | 210.3(2) | −0.1 | 208.8(2) | 208.4(3) | −0.4 | −1.6 | −1.9 | $\delta(F_1Xe_1F_2)_{i.p.}$ |
| 194.6(4),br | 186.4(4),br | −8.2 | 187.6(4),br | 181.6(4),br | −6.0 | −7.0 | −4.8 | $\rho_r(HO_1Xe_1F_1F_2)_{o.o.p.}$ |
| 122.3(3) | 121.0(4) | −1.3 | 121.8(5) | 120.3(7) | −1.5 | −0.5 | −0.7 | } lattice modes |
| 106.3(14) | 106.1(14) | −0.2 | 106.2(15) | 106.1(15) | −0.1 | 0.1 | 0.0 | |

[a]Frequencies are given in cm$^{-1}$. [b]Values in parentheses denote relative Raman intensities. [c]Raman spectra were recorded in FEP sample tubes at −150 °C using 1064-nm excitation. The abbreviations denote broad (br) and not observed (n.o.). Weak bands at 611.7(5) and 607.6(5) in the spectra (not listed) are assigned to $[XeF][AsF_6]$ (see ref 8). [d]The abbreviations denote stretch ($\nu$), bend ($\delta$), wag ($\rho_w$), rock ($\rho_r$), in-plane (i.p.), and out-of-plane (o.o.p.). The in-plane and out-of-plane mode descriptions refer to the $XeOF_2$ plane (Figure 8). [e]The band intensity has been corrected for overlap with a FEP band occuring at 381 cm$^{-1}$. [f]The band intensity has been corrected for overlap with the 610 cm$^{-1}$ band of $[XeF][AsF_6]$ (see ref 8).

**Table 5. Experimental Raman Frequencies[a] and Intensities[b] for $[FXe^{16/18}OXeF_2][PnF_6]$ (Pn = As, Sb)[c]**

| SbF₆ | AsF₆ | | | |
|---|---|---|---|---|
| $^{16}O$ | $^{16}O$ | $^{18}O$[d] | $^{16/18}\Delta\nu$ | assignment[e] |
| 658.7(12) | 691.2(12) | 691.3(13) | 0.1 | } $\nu_1(A_{1g})(PnF_6^-)$ |
| 635.3(3) | 673.7(2) | 673.5(3) | −0.2 | |
| 643.3(9) | 645.4(10) | 615.6(12) | −29.8 | $\nu(Xe_1O_1) - \nu(Xe_2O_1)$ |
| 587.6(1) | 586.2(1) | 587.1 sh | 0.9 | } $\nu_2(E_g)(PnF_6^-)$ |
| 575.7(2) | 577.1(2) | 577.2(3)[f] | 0.2 | |
| 554.2(2) | 556.0(3) | 555.0 sh | −1.0 | } $\nu(Xe_2F_3)$ |
| 544.2(98) | 545.6(84) | 545.6(89) | 0.0 | |
| 512.3(100) | 513.5(100) | 511.1(100) | −2.4 | $\nu(Xe_1F_1) + \nu(Xe_1F_2)$ |
| 404.6(7) | 409.4(5) | 390.3(5) | −19.1 | } $\nu(Xe_1O_1) + \nu(Xe_2O_1)$ |
| | 405.1(6) | 384.0(6) | −21.1 | |
| 286.5(3) | 397.0(2) | | | |
| 284.3 sh | 373.9(3) | 373.8 sh | −0.1 | } $\nu_5(T_{2g})(PnF_6^-)$ |
| 272.6(1 | 360.1(1) | 359.8(1) | −0.2 | |
| 292.5(6) | 300.6(8) | 290.0(7) | −10.6 | $\delta(OXe_1F_1) - \delta(OXe_1F_2)$ |
| 228.3(4) | 229.9(2) | 229.6(3) | −0.3 | } $\delta(F_1Xe_1F_2)_{o.o.p.}$ |
| 208.2(4) | 225.6(1) | 225.6(1) | 0.0 | |
| 183.0 sh | 187.7(2) | 187.6(2) | −0.1 | } $\delta(F_1Xe_1F_2)_{i.p.}$ |
| 180.7(4) | 181.3(4) | 181.1(4) | −0.2 | |
| 173.4(3) | 174.7(2) | 173.9(2) | −0.8 | |
| 168.1(2) | 155.7(1) | 155.5(1) | −0.2 | |
| 147.1(1) | 132.9(3) | 132.4(3) | −0.5 | |
| 129.2(4) | 119.8(2) | 120.3(2) | 0.5 | deformation modes[g] |
| 108.1 sh | 114.2(4) | 114.3(4) | 0.1 | |
| 104.1(5) | 106.2(4) | 105.4(7) | −0.8 | |
| 95.4 sh | 97.2(5) | 96.9(7) | −0.3 | |
| 74.9(6) | 76.0(8) | 75.7(12) | −0.3 | |
| 71.4 sh | 71.3(7) | 71.6(9) | 0.3 | |

[a]Frequencies are given in cm$^{-1}$. [b]Values in parentheses denote relative Raman intensities. [c]Raman spectra were recorded in FEP sample tubes at −150 °C using 1064-nm excitation. The abbreviation denotes a shoulder (sh). [d]A weak band at 498.5(3) in the $^{18}O$ spectrum is attributed to $[FXe^{18}OXe(F)_2{}^{18}OXeF_2][AsF_6]$. [e]The abbreviations denote stretch ($\nu$), bend ($\delta$), in-plane (i.p.), and out-of-plane (o.o.p.). The in-plane and out-of-plane mode descriptions refer to the $XeOF_2$ plane (Figure 8). [f]The band intensity has been corrected for overlap with a FEP band occurring at 578 cm$^{-1}$. [g]These modes are not individually described because they are strongly coupled and give rise to complex mode descriptions.

NBO parameters for the terminal $^{IV}Xe_3O_2F_{4,5}$ and $^{II}Xe_2O_1$ groups are not explicitly discussed but closely follow the trends already discussed in the $[FXe^{II}OXe^{IV}F_2][PnF_6]$ (Pn = As, Sb) section for $XeOF_2$, $HOXeF_2^+$, and $F^{II}XeO^{IV}XeF_2^+$. Owing to

**Table 6. Experimental Raman Frequencies[a] and Intensities[b] for $[H^{16/18}OXe(F)_2{}^{16/18}OXeF_2][AsF_6]^c$**

| $^{16}O$[d] | $^{18}O$[d] | $^{16/18}\Delta\nu$ | assignment[e] |
|---|---|---|---|
| 695.6(3) | 695.7(2) | 0.1 | } $\nu_1(A_{1g})(AsF_6^-)$ |
| 688.6(11) | 688.7(8) | 0.1 | |
| 681.4(6)[f] | 681.3(5) | −0.1 | |
| 675.4(4) | 676.0 sh | 0.6 | |
| 658.1(3), br | 624.6(1), br | −33.5 | $[\nu(Xe_3O_2) -\nu(Xe_1O_2)] + \nu(Xe_1O_1)$ |
| 586.8(2) | 586.8(2) | 0.0 | } $\nu_2(E_g)(AsF_6^-)$ |
| 579.2(7) | 579.2(7) | 0.0 | |
| 573.6(5) | 573.8(4) | −0.2 | |
| 569.1(7) | 569.1(6) | 0.0 | |
| 559.4(82) | 558.9(62) | −0.5 | } $\nu(Xe_1F_1) + \nu(Xe_1F_2)$ |
| 549.7(9) | 549.8(9) | 0.1 | |
| 545.9(13) | 546.1(11) | 0.2 | |
| 536.1(22) | 535.6(21) | −0.5 | |
| 510.5 sh | 510.2 sh | −0.3 | } $\nu(Xe_3F_4) + \nu(Xe_3F_5)$ |
| 507.3(100) | 506.8(100) | −0.5 | |
| 436.4(2)[g] | 438.1(1)[g] | 1.7 | |
| 422.9(9) | 406.5(4) | −16.4 | } $\delta(O_2Xe_3F_4) - \delta(O_2Xe_3F_5)$ |
| 418.2(4) | 395.2(2) | −23.0 | |
| 374.5(4) | 373.9(3) | −0.6 | } $\nu_5(T_{2g})(AsF_6^-)$ |
| 370.0(2) | 370.4(3) | 0.4 | |
| 366.6(2) | 366.4(1) | −0.2 | |
| 281.4(2) | 278.8(1) | −2.6 | } $\delta(O_1Xe_1F_1) - \delta(O_1Xe_1F_2)$ |
| 268.5(3) | 265.3(2) | −3.2 | |
| 241.4(2) | 237.5(3) | −3.9 | |
| 221.5(1) | 221.9(1) | 0.4 | $\delta(F_4Xe_3F_5)_{i.p.} + \delta(F_1Xe_1F_2)_{o.o.p.}$ |
| 173.5(7), br | 171.4(6), br | −2.1 | $\delta(F_1Xe_1F_2)_{i.p.} + \delta(F_4Xe_3F_5)_{i.p.}$ |
| 142.2(5) | 140.7(5) | −1.5 | } lattice modes |
| 118.2(8) | 116.9(8) | −1.3 | |

[a]Frequencies are given in cm$^{-1}$. [b]Values in parentheses denote relative Raman intensities. [c]Raman spectra were recorded in FEP sample tubes at −150 °C using 1064-nm excitation. The abbreviations denote shoulder (sh) and broad (br). [d]Weak bands observed at 598.1(1), 554.4 sh, and 479.7(2) in the $^{16}O$ spectrum and at 479.3(1) in the $^{18}O$ spectrum are assigned to $Xe_3OF_3^+$.[18] [e]The abbreviations denote stretch ($\nu$), bend ($\delta$), in-plane (i.p.), and out-of-plane (o.o.p.). The in-plane and out-of-plane mode descriptions refer to the corresponding $XeOF_2$ plane (Figure 8). [f]The band intensity has been corrected for overlap with the 681 cm$^{-1}$ band of the $AsF_6^-$ anion of $[Xe_3OF_3][AsF_6]$.[18] [g]Unassigned bands.

**Table 7. Experimental Raman Frequencies[a] and Intensities[b] for $[FXe^{16/18}OXe(F)_2{}^{16/18}OXeF_2][AsF_6]^c$**

| $^{16}O$ | $^{18}O$ | $^{16/18}\Delta\nu$ | assignment[d] |
|---|---|---|---|
| 700.8(3) | 700.8(3) | 0.0 | } $\nu_1(A_{1g})$ ($AsF_6^-$) |
| 679.1(7) | 679.1(15) | 0.0 | |
| 662.4(1) br | 632.1(1) br | −30.3 | $[\nu(Xe_3O_2) - \nu(Xe_1O_2)] + [\nu(Xe_1O_1) - \nu(Xe_2O_1)]$ |
| 577.1(4) | 576.9(7) | −0.2 | $\nu_2(E_g)$ ($AsF_6^-$) |
| 550.3(46) | 550.2(45) | −0.1 | $\nu(Xe_2F_3)$ |
| 539.4(5) | 539.3(5) | −0.1 | } $[\nu(Xe_1F_1) + \nu(Xe_1F_2)] + [\nu(Xe_3F_4) + \nu(Xe_3F_5)]$ |
| 534.0 sh | 533.5 sh | −0.5 | |
| 526.7(16) | 525.5(15) | −1.2 | |
| 513.6(3)[e] | 510.6(3)[e] | −3.0 | } $[\nu(Xe_1F_1) + \nu(Xe_1F_2)] - [\nu(Xe_3F_4) + \nu(Xe_3F_5)]$ |
| 498.6(100) | 498.7(100) | 0.1 | |
| 409.9(1)[f] | 409.9(1)[f] | 0.0 | |
| 375.5(5) | 375.6(4) | 0.1 | } $\nu_5(T_{2g})$ ($AsF_6^-$) |
| 366.6(2) | 366.7(2) | 0.1 | |
| 344.7(3) br | 329.7(3) br | −15.0 | $\delta(O_2Xe_3F_4) - \delta(O_2Xe_3F_5)$ |
| 299.2 sh | 287.8 sh | −11.4 | $\delta(O_1Xe_1F_1) - \delta(O_1Xe_1F_2)$ |
| 214.7(2) | 214.9(2) | 0.2 | $\delta(F_4Xe_3F_5)_{i.p.} + \delta(F_1Xe_1F_2)_{o.o.p.}$ |
| 201.7(2) | 201.9(4) | 0.2 | $\delta(F_4Xe_3F_5)_{i.p.} + \delta(F_1Xe_1F_2)_{i.p.}$ |
| 165.8(1)[g] | 164.2(2) | −1.6 | $\delta(F_3Xe_2O_1)_{i.p.} + \delta(F_1Xe_1F_2)_{i.p.}$ |
| 159.0(1) | 159.0(1) | 0.0 | $\delta(F_3Xe_2O_1)_{i.p.} - [\delta(F_1Xe_1F_2)_{i.p.}]_{small}$ |
| 117.5(2) | 117.0(2) | −0.5 | } lattice modes |
| 104.0(6) | 103.6(6) | −0.4 | |

[a]Frequencies are given in $cm^{-1}$. [b]Values in parentheses denote relative Raman intensities. [c]Raman spectra were recorded in FEP sample tubes at −150 °C using 1064-nm excitation. The abbreviations denote shoulder (sh) and broad (br). [d]The abbreviations denote stretch ($\nu$), bend ($\delta$), in-plane (i.p.), and out-of-plane (o.o.p.). The in-plane and out-of-plane mode descriptions refer to the corresponding $XeOF_2$ plane (Figure 8). [e]These bands may arise from $FXe^{16}OXeF_2^+$. [f]Unassigned bands. [g]The band intensity has been corrected for overlap with the $Xe^{16}OF_2\cdot nHF$ band occurring at 166.0 $cm^{-1}$ (see ref 3).
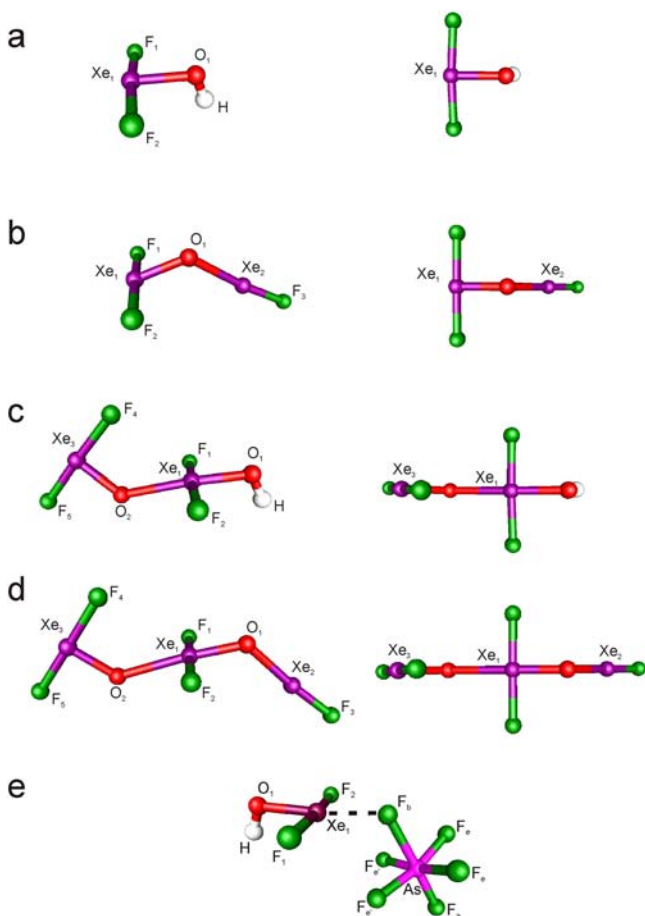


Figure 8. Calculated geometries [B3LYP/aug-cc-pVTZ(-PP)] for (a) $HOXeF_2^+$, (b) $FXeOXeF_2^+$, (c) $HOXe(F)_2OXeF_2^+$, (d) $FXeOXe(F)_2OXeF_2^+$, and (e) $[HOXeF_2][AsF_6]$. Geometrical parameters are provided in Table S8 (Supporting Information).

strong coupling of the $^{IV}Xe_1O_{1,2}F_{1,2}$ groups with the terminal $^{IV}Xe_3O_2F_{4,5}$ and $^{II}Xe_2O_1$ groups, clear correlations between frequencies and NBO parameters are not readily apparent.

As in the cases of $HOXeF_2^+$ and $FXeOXeF_2^+$, the Raman spectra of $[HOXe(F)_2OXeF_2][AsF_6]$ and $[FXeOXe(F)_2OXeF_2][AsF_6]$ are very similar. In general, the vibrational frequencies of the latter chain cations occur at frequencies similar to the corresponding modes in their parent cations. Only three bands, corresponding to a stretch and two bends, display significant $^{16/18}O$-isotopic dependencies in $[FXeOXe(F)_2OXeF_2][AsF_6]$. Three related bands are observed in $[HOXe(F)_2OXeF_2][AsF_6]$; however, both bending modes are likely factor-group split. The highest frequency $^{16/18}O$-dependent modes occur at 658.1 and 662.4 $cm^{-1}$ with isotopic shifts of −33.5 and −30.3 $cm^{-1}$ for $HOXe(F)_2OXeF_2^+$ and $FXeOXe(F)_2OXeF_2^+$, respectively. These bands are assigned to the coupled Xe−O stretches, $\{[\nu(^{IV}Xe_3O_2) - \nu(^{IV}Xe_1O_2)] + \nu(^{IV}Xe_1O_1)\}$ and $\{[\nu(^{IV}Xe_3O_2) - \nu(^{IV}Xe_1O_2)] + [\nu(^{IV}Xe_1O_1) - \nu(^{II}Xe_2O_1)]\}$, respectively. Extensive vibrational coupling is not suggested by the calculated models of these cations where $\nu(^{IV}Xe_1O_1)$ $[\nu(^{IV}Xe_1O_1) - \nu(^{II}Xe_2O_1)$ in the case of $FXeOXe(F)_2OXeF_2^+]$ and $\nu(^{IV}Xe_3O_2) - \nu(^{IV}Xe_1O_2)$ occur at significantly different frequencies, although their calculated isotopic shifts and frequencies ($HOXe(F)_2OXeF_2^+$, 626.2 (−28.7), 685.1 (−33.5) $cm^{-1}$; $FXeOXe(F)_2OXeF_2^+$, 671.4 (−31.1), 708.1 (−34.9) $cm^{-1}$) are in good agreement with the experimental values. However, the gas-phase calculations for both cations do not take into account ion pairing with the $AsF_6^-$ anion, which would render $^{IV}Xe_3$ less electropositive and may lower $\nu(^{IV}Xe_3O_2) - \nu(^{IV}Xe_1O_2)$ sufficiently to allow the $\nu(^{IV}Xe_3O_2) - \nu(^{IV}Xe_1O_2)$ and $\nu(^{IV}Xe_1O_1)$ $[\nu(^{IV}Xe_1O_1) - \nu(^{II}Xe_2O_1)$ in the case of $FXeOXe(F)_2OXeF_2^+]$ stretches to couple.

The remaining two broad bands of both cations are $^{16/18}O$-dependent and are assigned to the coupled bending modes $\delta(O_2{}^{IV}Xe_3F_4) - \delta(O_2{}^{IV}Xe_3F_5)$ and $\delta(O_1{}^{IV}Xe_1F_1) - \delta(O_1{}^{IV}Xe_1F_2)$ with the former occurring at higher frequency.

These bands are split in $[HOXe(F)_2OXeF_2][AsF_6]$, appearing at 418.2 and 422.9 cm$^{-1}$ ($^{16/18}\Delta\nu$; $-23.0$, $-16.4$ cm$^{-1}$) and 241.4, 268.5, and 281.4 cm$^{-1}$ ($^{16/18}\Delta\nu$; $-3.9$, $-3.2$, $-2.6$ cm$^{-1}$), respectively. The corresponding $[FXeOXe(F)_2OXeF_2][AsF_6]$ bands occur at 344.7 and 299.2 cm$^{-1}$. The greater frequency differences between the corresponding bending modes in the hydroxyl cation and those of $[FXe(F)_2OXeF_2][AsF_6]$ and their $^{16/18}O$-isotopic shifts are well reproduced by the calculations (Tables S6 and S7, Supporting Information).

The remaining bands are insensitive to $^{16/18}O$-isotopic substitution. In the spectrum of $HOXe(F)_2OXeF_2^+$, the split bands at 536.1, 545.9, 549.7, and 559.4 cm$^{-1}$ are assigned to the $\nu(^{IV}Xe_1F_1) + \nu(^{IV}Xe_1F_2)$ mode, and the split bands at 507.3 and 510.5 cm$^{-1}$ are assigned to the $\nu(^{IV}Xe_3F_4) + \nu(^{IV}Xe_3F_5)$ mode. The corresponding modes in $FXeOXe(F)_2OXeF_2^+$ are also in-phase and out-of-phase coupled, appearing as split bands at 526.7, 534.0, and 539.4 cm$^{-1}$ and at 498.6 and 513.6 cm$^{-1}$, respectively, with the terminal $^{II}Xe_2-F_3$ stretching band occurring at 550.3 cm$^{-1}$. The only other bands that are observed in both salts are the coupled in-plane $F-^{IV}Xe-F$ bends. The bands at 214.7 ($FXeOXe(F)_2OXeF_2^+$) and 221.5 ($HOXe(F)_2OXeF_2^+$) cm$^{-1}$ are assigned to $\delta(F_4{}^{IV}Xe_3F_5)_{i.p.} + \delta(F_1{}^{IV}Xe_1F_2)_{o.o.p.}$ and those at 173.5 ($HOXe(F)_2OXeF_2^+$) and 201.7 ($FXeOXe(F)_2OXeF_2^+$) cm$^{-1}$ are assigned to $\delta(F_1{}^{IV}Xe_1F_2)_{i.p.} + \delta(F_4{}^{IV}Xe_3F_5)_{i.p.}$.

Hydrogen/deuterium substitution in $[HOXe(F)_2OXeF_2]$-$[AsF_6]$ did not show isotopic dependencies in the Raman spectrum. It is likely that the hydrogen-dependent bands are too weak and broad to be observed by Raman spectroscopy.

**Computational Results.** The gas-phase geometries of $^{1/2}H^{16/18}OXeF_2^+$, $[^{1/2}H^{16/18}OXeF_2][AsF_6]$, $H^{16/18}OXe(F)_2{}^{16/18}OXeF_2^+$, $FXe^{16/18}OXeF_2^+$, $FXe^{16/18}OXe(F)_2{}^{16/18}OXeF_2^+$, $XeF_3^+ \cdot HF$, and $[XeF_3][AsF_6]$ were optimized starting from $C_1$ symmetries (square brackets designate ion pairs; Figures 8 and 9 and Tables S2 and S8,
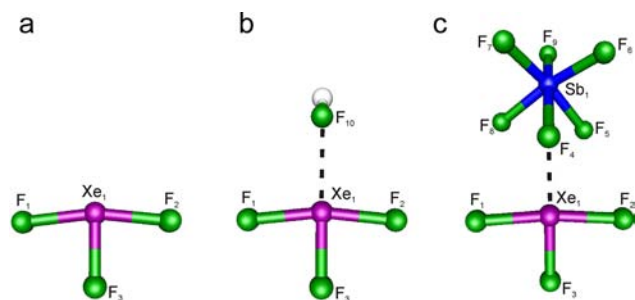


**Figure 9.** Calculated geometries [B3LYP/aug-cc-pVTZ(-PP)] of (a) $XeF_3^+$, (b) $XeF_3^+ \cdot HF$, and (c) $[XeF_3][AsF_6]$. Calculated and experimental geometrical parameters are provided in Tables 3 and S2 (Supporting Information).

Supporting Information). All of the structures resulted in stationary points with all frequencies real. The PBE1PBE/aug-cc-pVTZ(-PP), B3LYP/aug-cc-pVTZ(-PP), and MP2/aug-cc-pVTZ(-PP) results reproduce the vibrational frequency trends across the series of compounds reported in this work (see the Discussion; Raman Spectroscopy). The ranges of geometrical parameters cited below correspond to the aforementioned methods. In the case of $XeF_3^+ \cdot HF$, two starting geometries were optimized: (1) square-planar $XeF_4$ and a nearby, out-of-plane $H^+$ ion (F---H, 2.840 Å), and (2) T-shaped $XeF_3^+$ and a nearby HF molecule with the F atom coplanar with $XeF_3^+$ and the H

atom out of the $XeF_3$ plane (Xe---F, 2.941 Å). Both starting geometries optimized to $F_3Xe$---$FH^+$ (Xe---F, 2.537−2.556 Å), indicating that this is a better description than $F_3XeF$---$H^+$. This is supported by the similarities between the experimental and calculated geometrical parameters of $XeF_3^+$ and those of $F_3Xe$---$FH^+$.

*$HOXeF_2^+$, $[HOXeF_2][AsF_6]$, and $FXe^{II}OXe^{IV}F_2^+$.* The $^{IV}Xe_1-O_1$ bond in $FXeOXeF_2^+$ (1.837−1.885 Å) is elongated relative to that of $XeOF_2$ (1.770−1.821 Å)[4] and even more so in $HOXeF_2^+$ (1.880−1.929 Å) and the $[HOXeF_2][AsF_6]$ ion pair (1.931−1.965 Å). Overall, the trend is consistent with electron density transfer from Xe$^{IV}$ and oxygen of $XeOF_2$ (cf. gas-phase $XeOF_2$ charges: O, $-0.81$; Xe$^{IV}$, 2.02) to the H/Xe$^{II}$ Lewis acid centers [charges: H (O, $-0.69$; Xe$^{IV}$, 2.18; H, 0.53)/ Xe$^{II}$ (O, $-0.84$; Xe$^{IV}$, 2.14; Xe$^{II}$, 1.24)], where the charges of the coordinated H and FXe ligands are compared with those of the gas-phase Lewis acids (H$^+$, 1.00; XeF$^+$, 1.33).

The increased $^{IV}Xe_1-O_1$ bond lengths correlate with their lower $^{IV}Xe_1-O_1$ bond orders (H derivative, 0.60; FXe derivative, 0.73) relative to that of $XeOF_2$ (0.79). The lower $^{IV}Xe_1-O_1$ bond orders also result in decreased $O_1-^{IV}Xe_1-F$ bond angles because of the reduced steric requirements of the $^{IV}Xe_1-O_1$ bond domains in the cations ($FXeOXeF_2^+$, 89.3−89.9°; $HOXeF_2^+$, 87.1−87.7°; $[HOXeF_2][AsF_6]$, 87.2−88.0°) relative to the Xe−O double bond domain of $XeOF_2$ (94.9−95.9°).[4] The $O_1-^{IV}Xe_1-F$ bond angles are also greater than the $F_{ax}-^{IV}Xe-F_{eq}$ bond angles of $XeF_3^+$ (83.3−84.2°; $^{IV}Xe-F_{eq}$ NBO bond order, 0.50) as a result of the larger $^{IV}Xe_1-O_1$ bond domain.

In contrast with the $^{IV}Xe_1-O_1$ bond length trends, the $^{IV}Xe_1-F$ bond lengths follow the reverse order and are shorter in the cations ($FXeOXeF_2^+$, 1.921−1.946 Å; $HOXeF_2^+$, 1.903−1.927 Å; $[HOXeF_2][AsF_6]$, 1.938−1.963 Å) than in $XeOF_2$ (1.968−1.997 Å),[4] but are longer than the related Xe−$F_{ax}$ bonds of $XeF_3^+$ (1.883−1.906 Å) (Table S2, Supporting Information).

The $^{II}Xe_2-O_1$ bond (2.240−2.296 Å) of $FXeOXeF_2^+$ is significantly longer than the $^{IV}Xe_1-O_1$ bond (1.837−1.885 Å), in accordance with the greater electronegativity of Xe(IV) relative to that of Xe(II). The $Xe_1-O_1-Xe_2$ bond angle (123.8−129.7°) is significantly more open than the $Xe_1-O_1-H$ bond angle (108.1°), which is likely a consequence of the Xe$^{II}$---Xe$^{IV}$ steric interaction (Xe$^{II}$---Xe$^{IV}$, 3.460−3.588 Å; compared to twice the van der Waals radius of Xe, 4.32 Å[50]), as well as the greater oxygen electron lone pair−bond pair interaction provided by the O−H bond (bond order, 0.61) relative to the more ionic Xe−F bond (bond order, 0.34).

*$HOXe^{IV}(F)_2OXe^{IV}F_2^+$ and $FXe^{II}OXe^{IV}(F)_2OXe^{IV}F_2^+$.* Coordination of a second $XeOF_2$ molecule to $HOXeF_2^+$ and to $FXeOXeF_2^+$ has very little effect on the calculated geometries of the $HOXeF_2$ and $FXeOXeF_2$ moieties of the title cations. The $^{IV}Xe_1-O_1$ and $^{IV}Xe_1-F_{1,2}$ bonds in $HOXe(F)_2OXeF_2^+$ (1.914−1.945 Å and 1.929−1.958 Å, respectively) and $FXeOXe(F)_2OXeF_2^+$ (1.863−1.899 Å and 1.922−1.962 Å, respectively) are slightly elongated relative to those of the parent cations, whereas the related bond angles remain essentially unchanged. The Xe atoms and the $O_1$, $O_2$, $F_4$, and $F_5$ atoms are coplanar in both cations, and the $F_1$ and $F_2$ atoms bonded to $^{IV}Xe_1$ are nearly perpendicular to this plane. The geometric parameters of the terminal $XeOF_2$ groups follow the trends observed in $HOXeF_2^+$ and $FXeOXeF_2^+$, that is, $^{IV}Xe_3-O_2$ bond elongation and $^{IV}Xe_3-F_{4,5}$ bond contraction.

There are no significant differences in $Xe^{II}/Xe^{IV}$ charges among the $H(OXeF_2)_n^+$ and $FXe(OXeF_2)_n^+$ ($n = 1, 2$) cation series (Table S9, Supporting Information), and there are no significant differences between the $Xe^{II}-F$ and $Xe^{II}-O$ bond orders of $FXe(OXeF_2)_n^+$. The oxygen and fluorine charges and the $Xe^{IV}-F$ and $Xe^{IV}-O$ bond orders of the terminal $OXeF_2$ groups in $HOXe(F)_2OXeF_2^+$ and $FXeOXe(F)_2OXeF_2^+$ are nearly equal. The terminal $^{IV}Xe_3O_2F_{4,5}$ groups of both cations ($^{IV}Xe_3-O_2$ bond orders, 0.71) are weakly coordinated to their adjacent $^{IV}Xe_1O_1F_{1,2}$ groups, as indicated by their small $^{IV}Xe_1-O_2$ bond orders (0.17 and 0.14, respectively). Correspondingly, the $^{IV}Xe_1O_1F_{1,2}$ group in $FXeOXe(F)_2OXeF_2^+$ ($^{IV}Xe_1-O_1$ bond order, 0.65) is weakly coordinated to the $^{II}Xe_2F_3$ group ($^{II}Xe_2-O_1$ bond order, 0.26).

*$XeF_3^+ \cdot HF$ and $[XeF_3][SbF_6]$.* As noted in the discussion of the experimental structure, coordination of HF to $XeF_3^+$ has very little effect on the calculated geometry of the $XeF_3$ group in $F_3Xe\text{---}FH^+$, which is also true for the atomic charges and for the Xe−F and H−F bond orders when compared with those of $XeF_3^+$ and HF (Table S9, Supporting Information). This is also consistent with the very low Xe---F bond order, 0.06. The $Xe-F_{eq}$ (1.839−1.870 Å) and $Xe-F_{ax}$ (1.892−1.916 Å) bond lengths of the adduct-cation are the same as those of $XeF_3^+$ ($Xe-F_{eq}$, 1.838−1.867 Å; $Xe-F_{ax}$, 1.883−1.906 Å) but slightly shorter than those of $[XeF_3][SbF_6]$ ($Xe-F_{eq}$, 1.894−1.921 Å; $Xe-F_{ax}$, 1.926−1.950 Å). The $F_{eq}-Xe-F_{ax}$ bond angles are also similar ($XeF_3^+$, 83.3−84.2°; $XeF_3^+ \cdot HF$, 83.7−84.7°; $[XeF_3]$-$[SbF_6]$, 86.0−86.8°). The poorest agreement between the calculated $F_3Xe\text{---}FH^+$ and $[XeF_3][SbF_6]$ geometries and their experimental geometries occurs for the contact angles and distances. In both models, the calculated $F_{eq}-Xe\text{---}F$ angles are ∼180° instead of the ∼160° angle observed in their respective crystal structures where additional secondary contacts occur. The Xe---F distances are overestimated and underestimated for $F_3Xe\text{---}FH^+$ and $[XeF_3][SbF_6]$, respectively (calcd; $F_3Xe\text{---}FH^+$, 2.537−2.556 Å; $[XeF_3][SbF_6]$, 2.127−2.136 Å), relative to those in their crystal structures (exptl; $F_3Xe\text{---}FH^+$, 2.462(2); $[XeF_3][SbF_6]$, 2.485(1) Å). The angle discrepancies presumably result from their deformabilities and are likely the result of crystal packing.[3,46]

## CONCLUSION

The Lewis base properties of oxygen in $XeOF_2$ have been demonstrated by the syntheses of $[^{1/2}H^{16/18}OXeF_2][AsF_6]$, $[H^{16/18}OXe(F)_2^{16/18}OXeF_2][AsF_6]$, $[FXe^{16/18}OXeF_2][AsF_6]$, and $[FXe^{16/18}OXe(F)_2^{16/18}OXeF_2][AsF_6]$ in high yields and purities. The salts are the first new Xe(IV) cations to have been synthesized in over 20 years, with the $[^{1/2}H^{16/18}OXeF_2][AsF_6]$ and $[H^{16/18}OXe(F)_2^{16/18}OXeF_2][AsF_6]$ salts also representing the only examples of xenon hydroxy derivatives to have been isolated and structurally characterized in the solid state. With the exception of $[H^{16/18}OXe(F)_2^{16/18}OXeF_2][AsF_6]$, which slowly decomposes at −78 °C, the aforementioned salts are kinetically stable at −78 °C but slowly decompose upon warming to between −50 and −35 °C. The decomposition pathways, inferred from their decomposition products, are supported by their Born−Fajans−Haber thermochemical cycles. The latter show the redox decomposition pathways are mainly driven by their reaction enthalpies (see Thermochemistry, Supporting Information).

In an attempt to isolate and structurally characterize $[HOXeF_2][SbF_6]$, a mixture of crystalline solvolysis products, $[XeF_3 \cdot HF][Sb_2F_{11}]$, $[H_5F_4][SbF_6] \cdot 2[XeF_3 \cdot HF][Sb_2F_{11}]$, and

$[XeF_3][SbF_6]$, were obtained upon dissolution of $XeOF_2 \cdot nHF$ in the superacidic medium, $HF/SbF_5$. The experimental and calculated geometries of the $XeF_3^+$ and $XeF_3 \cdot HF^+$ cations in $[XeF_3 \cdot HF][Sb_2F_{11}]$, $[H_5F_4][SbF_6] \cdot 2[XeF_3 \cdot HF][Sb_2F_{11}]$, and $[XeF_3][SbF_6]$ are very similar. The crystal structure of $[H_5F_4][SbF_6] \cdot 2[XeF_3 \cdot HF][Sb_2F_{11}]$ contains the previously unknown acidium cation $H_5F_4^+$ and the $F_3Xe\text{---}FH^+$ cation, a rare example of HF coordinated to a main-group center. Quantum-chemical calculations also support the adduct formulation, $F_3Xe\text{---}FH^+$.

## EXPERIMENTAL SECTION

**Caution.** The xenon(IV) oxide fluoride species $XeOF_2$, $[H(OXeF_2)_n][AsF_6]$, and $[FXe(OXeF_2)_n][AsF_6]$ ($n = 1, 2$) are highly energetic, shock-sensitive materials and are only stable at the low temperatures described in the experimental procedures that outline their syntheses. Xenon oxide difluoride can detonate at low temperatures when mechanically or thermally shocked. Thus, adequate protective apparel and working behind adequate shielding are crucial for the safe manipulation of these materials. In the case of $XeOF_2$, detonations may occur upon freezing or further cooling of its $CH_3CN$ solutions to −196 °C. It is strongly recommended that only small scale (<100 mg) syntheses of $XeOF_2$, $[H(OXeF_2)_n][AsF_6]$ and $[FXe(OXeF_2)_n][AsF_6]$ ($n = 1, 2$) be undertaken.

**Apparatus and Materials.** All manipulations involving air-sensitive materials were carried out under strictly anhydrous conditions as previously described.[51] Reaction vessels/Raman sample tubes were fabricated from lengths of $^{1}/_{4}$-in. o.d. FEP tubing that had been heat-sealed at one end and joined to Kel-F valves by means of 45° SAE compression fittings. In several instances, a T-shaped reactor was used that consisted of an ordinary valve and tube assembly with a side arm fused at right angles approximately one-third of the tube length from the valve. All reaction vessels and sample tubes were rigorously dried under dynamic vacuum prior to passivation with 1 atm of $F_2$ gas for 12 h prior to use. The following syntheses refer to the natural abundance ($^{16}O$, $^1H$) compounds. Syntheses of the $^{18}O$- ($^2H$)-enriched samples used similar amounts and the appropriate $^{18}O$- ($^2H$)-enriched starting materials, that is, $Xe^{18}OF_2 \cdot n^{1/2}HF$, $[H_3^{18}O][PnF_6]$, and DF ($^2HF$).

Arsenic pentafluoride,[52] $^2HF$,[3] $SbF_5$,[16] $Xe^{16/18}OF_2 \cdot n^{1/2}HF$,[3] $[XeF]$-$[PnF_6]$,[53] where Pn = As, Sb, and $[^{1/2}H_3^{16/18}O][PnF_6]$[54] were prepared and purified according to the literature methods. Anhydrous HF (Harshaw Chemical Co.) was purified by the standard literature method.[55] High-purity Ar or $N_2$ gas were used for backfilling vessels. Both $H_2^{18}O$ (MSD isotopes, 97.8 atom % $^{18}O$) and $D_2O$ (MSD isotopes, 99.8 atom % deuterium) were used without further purification.

*$[^{1/2}H^{16/18}OXeF_2][AsF_6]$.* In a typical synthesis, 25.4 mg (0.124 mmol) of $Xe^{16}OF_2 \cdot n^{1/2}HF$ was prepared in situ according to the literature method[3] and was suspended in approximately 0.3 mL of aHF or aDF in a $^{1}/_{4}$-in. o.d. FEP T-shaped reaction tube that was connected to a Kel-F valve. The suspension froze at −196 °C, and 0.140 mmol of $AsF_5$ was condensed into the reactor. The reaction mixture was then warmed to −78 °C, mixed, and allowed to stand at −78 °C for 12 h to ensure complete reaction. The solvent was then removed under dynamic vacuum at −78 °C, leaving behind a white, microcrystalline powder that was stable for at least 4 weeks when stored at −78 °C in the absence of moisture. It is important to ensure that $XeOF_2$ is fully solvated to $XeOF_2 \cdot nHF$ prior to the addition of $AsF_5$, otherwise rapid and extensive decomposition to $[XeF][AsF_6]$ ensues.

*$[^{1/2}H^{16/18}OXe(F)_2^{16/18}OXeF_2][AsF_6]$.* The most efficient synthesis of the title compound was achieved by suspending 33.1 mg (0.161 mmol) of $Xe^{16}OF_2 \cdot n^{1/2}HF$, prepared in situ, in approximately 0.3 mL of anhydrous $^{1/2}HF$ in a $^{1}/_{4}$-in. o.d. FEP T-shaped reactor that had been connected to a Kel-F valve. The sample was introduced into the drybox by means of a cryowell without allowing it to warm above −78 °C, whereupon the $^{1/2}HF$ solvent was frozen in the cryowell (−120 °C). The frozen sample was opened, and 16.8 mg (0.0805 mmol) of

5101

dx.doi.org/10.1021/ja312493j | *J. Am. Chem. Soc.* 2013, 135, 5089−5104

$[^{1/2}H_3{}^{16/18}O][AsF_6]$ was added. The sample was resealed and immediately removed cold from the drybox, without significant warming, and placed in a −78 °C bath where the reagents were thoroughly mixed and allowed to react for 12 h. Within several minutes, the light yellow color of the sample began to intensify, and after the reaction was complete, the color was bright yellow. Removal of the solvent under dynamic vacuum at −78 °C resulted in a yellow powder. The attempted synthesis of the $SbF_6^-$ analogue using the same procedure resulted in decomposition within several minutes to $[Xe_3OF_3][SbF_6]$ with no evidence for $[HOXe(F)_2OXeF_2][SbF_6]$ formation.

*$[FXe^{16/18}OXeF_2][PnF_6]$ (Pn = As, Sb).* A $^1/_4$-in. o.d. FEP T-shaped reactor was connected to a Kel-F valve, and 46.3 mg (0.226 mmol) of $Xe^{16}OF_2 \cdot nHF$ was prepared in situ in approximately 0.3 mL of aHF. The sample was transferred cold into the drybox (as described above in the section relating to $[^{1/2}H^{16/18}OXeF_2][AsF_6]$) and was maintained at approximately −120 °C in a cryowell. To a reactor, 86.0 mg (0.253 mmol) of $[XeF][AsF_6]$ [93.4 mg (0.242 mmol) for the Sb salt] was added, and the reactor and contents were removed cold from the drybox and placed in a −78 °C bath where, over the course of 5−10 min, the color of the undissolved solid intensified to bright yellow. The reaction required approximately 1 week, with periodic agitation, to go to completion, resulting in a bright yellow solid under HF. In contrast, samples containing $^{18}O$ required up to 1 month to go to completion. Removal of the solvent under dynamic vacuum at −78 °C resulted in yellow powders.

*$[FXe^{16/18}OXe(F)_2{}^{16/18}OXeF_2][AsF_6]$.* The synthesis of $[FXe^{16/18}OXe(F)_2{}^{16/18}OXeF_2][AsF_6]$ was analogous to that of $[FXe^{16}OXeF_2][AsF_6]$. In a typical synthesis, 60.5 mg (0.295 mmol) of $Xe^{16/18}OF_2 \cdot nHF$ was allowed to react with 26.5 mg (0.0782 mmol) of $[XeF][AsF_6]$ in approximately 0.3 mL of aHF at −78 °C. Unlike $[FXe^{16}OXeF_2][AsF_6]$, $[FXe^{16}OXe(F)_2{}^{16}OXeF_2][AsF_6]$ required 2 weeks to go to completion with periodic agitation, whereas $^{18}O$-enriched samples required at least 1 month. In each case, removal of the solvent under dynamic vacuum at −78 °C resulted in a yellow powder. Attempts to synthesize the analogous $SbF_6^-$ salts using $[XeF][SbF_6]$ proved unsuccessful, resulting in mixtures of $[FXeOXeF_2][SbF_6]$ and $XeOF_2 \cdot nHF$.

**X-ray Crystallography.** *Crystal Growth.* Crystals of $[H_5F_4]$-$[SbF_6] \cdot 2[XeF_3 \cdot HF][Sb_2F_{11}]$, $[XeF_3 \cdot HF][Sb_2F_{11}]$, and $[XeF_3][SbF_6]$ were obtained as a mixture in a $^1/_4$-in. o.d. FEP T-shaped reaction vessel. Approximately 0.15 mL (∼17 mol %) of $SbF_5$ in HF was cooled to −78 °C and poured through a $^1/_4$-in. Teflon Swagelok union onto frozen HF (0.15 mL; −196 °C) containing 11.7 mg (0.0569 mmol) of $XeOF_2 \cdot nHF$. The sample was warmed to −78 °C and was well mixed before warming to −50 °C to dissolve the solid. The solution was cooled to −78 °C, and over the course of 24 h, colorless crystals formed. The reaction vessel was maintained at −78 °C while the supernatant was decanted into the side arm of the reaction vessel, which was also maintained at −78 °C. The side arm containing the supernatant was then cooled to −196 °C and heat-sealed under dynamic vacuum. Residual HF solvent was removed from the crystalline sample by pumping under dynamic vacuum at −78 °C. The dried sample was stored at −78 °C until suitable crystals could be selected and mounted on the X-ray diffractometer.

*Crystal Selection and Mounting.* The crystals were dumped into an aluminum trough cooled to −110 ± 5 °C by a cold stream of dry $N_2$ gas. This allowed selection of individual crystals from the bulk sample mixture as previously described.[56] Single crystals were mounted on glass fibers at −110 ± 5 °C using a Fomblin oil as the adhesive. The crystals used for data collection were as follows: $[XeF_3][SbF_6]$, a pale-yellow to colorless, transparent block measuring 0.29 × 0.26 × 0.21 mm³; $[H_5F_4][SbF_6] \cdot 2[XeF_3 \cdot HF][Sb_2F_{11}]$, a colorless, transparent plate measuring 0.32 × 0.21 × 0.12 mm³; $[XeF_3 \cdot HF][Sb_2F_{11}]$, a colorless, transparent needle measuring 0.26 × 0.08 × 0.05 mm³.

*Collection and Reduction of the X-ray Data.* Single crystals were centered on a Bruker AXS SMART APEX II diffractometer, equipped with a 4K CCD area detector and a triple-axis goniometer, controlled by the APEX2 graphical user interface (GUI) software,[57] using graphite-monochromated Mo Kα radiation (λ = 0.71073 Å). The diffraction data collections consisted of full φ rotations at fixed χ = 54.74° with (1010) 0.36° frames, followed by series of short (250 frames) ω scans at various φ settings to fill the gaps. The crystal-to-detector distance was 4.952 cm. The data collections were carried out in a 512 pixel × 512 pixel mode using 2 pixel × 2 pixel binning. Processing was carried out by using the APEX2 GUI software,[57] which applied Lorentz and polarization corrections to three-dimensionally integrated diffraction spots. The program SADABS[58] was used for scaling the diffraction data, the application of a decay correction, and an empirical absorption correction based on redundant reflections.

*Solution and Refinement of the Structures.* The XPREP[59] program was used to confirm the unit cell dimensions and the crystal lattices. The $[H_5F_4][SbF_6] \cdot 2[XeF_3 \cdot HF][Sb_2F_{11}]$, $[XeF_3 \cdot HF][Sb_2F_{11}]$, and $[XeF_3][SbF_6]$ structures were solved in the space groups $P\bar{1}$, $C2/c$, and $P2_1/c$, respectively, by use of direct methods, and the solutions yielded all atomic positions except those of hydrogen. In each case, the final refinement was obtained by introducing anisotropic parameters for all the atoms, an extinction parameter, and the recommended weight factor. The maximum electron densities in the final difference Fourier maps were located around the xenon atoms. The PLATON program[60] could not suggest additional or alternative symmetries.

**Raman Spectroscopy.** Raman spectra were recorded on a Bruker RFS 100 FT-Raman spectrometer at −150 °C using 1064-nm excitation, 300 mW laser power, and 1 cm⁻¹ resolution as previously described.[56]

**Computational Results.** The optimized geometries and frequencies of $H^{16/18}OXeF_2{}^+$, $[H^{16/18}OXeF_2][AsF_6]$, $H^{16/18}OXe(F)_2{}^{16/18}OXeF_2{}^+$, $FXe^{16/18}OXeF_2{}^+$, and $FXe^{16/18}OXe(F)_2{}^{16/18}OXeF_2{}^+$ were initially calculated at the MP2, B3LYP, and PBE1PBE levels of theory using aug-cc-pVTZ for H, O, and F and aug-cc-pVTZ-(PP) for Xe and As basis sets. The standard all-electron aug-cc-pVTZ basis sets, as implemented in the Gaussian program, were utilized for H, O, and F. Basis sets for Xe and As were obtained online from the EMSL Basis Set Exchange (https://bse.pnl.gov/bse/portal).[61] Quantum-chemical calculations were carried out using the programs Gaussian 03[62] and Gaussian 09[63] for geometry optimizations, vibrational frequencies, and Raman and infrared intensities. The program GaussView[64] was used to visualize the vibrational displacements that form the basis for the vibrational mode descriptions given in Tables 4−7 and S3−S7 (Supporting Information).

## ■ ASSOCIATED CONTENT

### ⓈSupporting Information

Complementary discussion of the thermochemistry; references for the supporting thermochemistry section; estimated volumes, lattice enthalpies, and entropies for $[XeOF][AsF_6]$, $[HOXeF_2][AsF_6]$, $[HOXe(F)_2OXeF_2][AsF_6]$, $[FXeOXeF_2]$-$[AsF_6]$, $[FXeOXe(F)_2OXeF_2][AsF_6]$, $[XeF][AsF_6]$, $[Xe_2F_3]$-$[AsF_6]$, $[Xe_3OF_3][AsF_6]$, and $[H_3O][AsF_6]$ (Table S1); calculated bond lengths and bond angles for $XeF_3{}^+$ and $XeF_3{}^+ \cdot HF$ and a complete list of experimental solid-state geometrical parameters for $[H_5F_4][SbF_6] \cdot 2[XeF_3 \cdot HF][Sb_2F_{11}]$, $[XeF_3 \cdot HF][Sb_2F_{11}]$, and the $[XeF_3][SbF_6]$ ion pair (Table S2); crystal packing for $[H_5F_4][SbF_6] \cdot 2[XeF_3 \cdot HF][Sb_2F_{11}]$ (Figure S1); crystal packing for $[XeF_3 \cdot HF][Sb_2F_{11}]$ (Figure S2); calculated vibrational frequencies and IR and Raman intensities for $HOXeF_2{}^+$ (Table S3), the $[HOXeF_2][AsF_6]$ ion pair (Table S4), $FXeOXeF_2{}^+$ (Table S5), $HOXe(F)_2OXeF_2{}^+$ (Table S6), and $FXeOXe(F)_2OXeF_2{}^+$ (Table S7); calculated bond lengths and bond angles for $HOXeF_2{}^+$, $FXeOXeF_2{}^+$, $HOXe(F)_2OXeF_2{}^+$, and $FXeOXe(F)_2OXeF_2{}^+$ and the $[HOXeF_2][AsF_6]$ ion pair (Table S8); NBO valencies, bond orders, and charges (NPA) for $HOXeF_2{}^+$ and $FXeOXeF_2{}^+$ (Table S9); complete refs 62 and 63; X-ray crystallographic files in CIF format for the structure determinations of $[H_5F_4][SbF_6]$

$\cdot 2[XeF_3 \cdot HF][Sb_2F_{11}]$, $[XeF_3 \cdot HF][Sb_2F_{11}]$, and $[XeF_3][SbF_6]$. This material is available free of charge via the Internet at http://pubs.acs.org.

## ■ AUTHOR INFORMATION

**Corresponding Author**
schrobil@mcmaster.ca
**Notes**
The authors declare no competing financial interest.

## ■ ACKNOWLEDGMENTS

## ■ REFERENCES

(1) Schrobilgen, G. J.; Brock, D. S.; Mercier, H. P. A. Noble-Gas Compounds. In *Kirk-Othmer Encyclopedia of Chemical Technology*, 5th ed.; John Wiley & Sons, Inc.: Hoboken, NJ, 2012, 1−21.

(2) Gerken, M.; Schrobilgen, G. J. *Coord. Chem. Rev.* **2000**, *197*, 335−395.

(3) Brock, D. S.; Bilir, V.; Mercier, H. P. A.; Schrobilgen, G. J. *J. Am. Chem. Soc.* **2007**, *129*, 3598−3611.

(4) Brock, D. S.; Mercier, H. P. A.; Schrobilgen, G. J. *J. Am. Chem. Soc.* **2010**, *132*, 10935−10943.

(5) Williamson, S. M.; Koch, C. W. *Science* **1963**, *139*, 1046−1047.

(6) Appelman, E. H.; Malm, J. G. *J. Am. Chem. Soc.* **1964**, *86*, 2141−2148.

(7) Frohn, H.-J.; Leblond, N.; Lutar, K.; Žemva, B. *Angew. Chem., Int. Ed.* **2000**, *39*, 391−393.

(8) Elliott, H. A.; Lehmann, J. F.; Mercier, H. P. A.; Jenkins, D. B.; Schrobilgen, G. J. *Inorg. Chem.* **2010**, *49*, 8504−8523.

(9) Gillespie, R. J.; Landa, B.; Schrobilgen, G. J. *Inorg. Chem.* **1976**, *15*, 1256−1263.

(10) Gillespie, R. J.; Schrobilgen, G. J. *Inorg. Chem.* **1974**, *13*, 2370−2374.

(11) Gillespie, R. J.; Landa, B.; Schrobilgen, G. J. *J. Chem. Soc. D* **1971**, 1543−1544.

(12) Schrobilgen, G. J.; Holloway, J. H.; Granger, P.; Brevard, C. *Inorg. Chem.* **1978**, *17*, 980−987.

(13) McKee, D. E.; Adams, C. J.; Bartlett, N. *Inorg. Chem.* **1973**, *12*, 1722−1725.

(14) McKee, D. E.; Zalkin, A.; Bartlett, N. *Inorg. Chem.* **1973**, *12*, 1713−1717.

(15) Boldrini, P.; Gillespie, R. J.; Ireland, P. R.; Schrobilgen, G. J. *Inorg. Chem.* **1974**, *13*, 1690−1694.

(16) Syvret, R. G.; Mitchell, K. M.; Sanders, J. C. P.; Schrobilgen, G. J. *Inorg. Chem.* **1992**, *31*, 3381−3385.

(17) Fir, B. A.; Gerken, M.; Pointner, B. E.; Mercier, H. P. A.; Dixon, D. A.; Schrobilgen, G. J. *J. Fluorine Chem.* **2000**, *105*, 159−167.

(18) Gerken, M.; Moran, M. D.; Mercier, H. P. A.; Pointner, B. E.; Schrobilgen, G. J.; Hoge, B.; Christe, K. O.; Boatz, J. A. *J. Am. Chem. Soc.* **2009**, *131*, 13474−13489.

(19) Bartlett, N.; Zalkin, A.; Leary, K. *Inorg. Chem.* **1974**, *13*, 775−779.

(20) Žemva, B. *Croat. Chem. Acta* **1988**, *61*, 163−187.

(21) Pointner, B. E.; Suontamo, R. J.; Schrobilgen, G. J. *Inorg. Chem.* **2006**, *45*, 1517−1534.

(22) Žemva, B.; Jesih, A.; Templeton, D. H.; Zalkin, A.; Cheetham, A. K.; Bartlett, N. *J. Am. Chem. Soc.* **1987**, *109*, 7420−7427.

(23) Tavčar, G.; Žemva, B. *Angew. Chem., Int. Ed.* **2009**, *48*, 1432−1434.

(24) Schrobilgen, G. J.; Martin-Rovet, D.; Charpin, P.; Lance, M. *J. Chem. Soc., Chem. Commun.* **1980**, *19*, 894−897.

(25) Holloway, J. H.; Kaučič, V.; Martin-Rovet, D.; Russell, D. R.; Schrobilgen, G. J.; Selig, H. *Inorg. Chem.* **1985**, *24*, 678−683.

(26) Kläning, U. K.; Appelman, E. H. *Inorg. Chem.* **1988**, *27*, 3760−3762.

(27) Downey, G. D.; Claassen, H. H.; Appelman, E. H. *Inorg. Chem.* **1971**, *10*, 1817.

(28) Jaselskis, B. *Science* **1964**, *146*, 263−264.

(29) Holloway, J. H. *Talanta* **1967**, *14*, 871−873.

(30) Margraff, R.; Adloff, J. P. *J. Chromatogr.* **1967**, *26*, 555−556.

(31) Claassen, H. H.; Knapp, G. *J. Am. Chem. Soc.* **1964**, *86*, 2341−2342.

(32) Reuben, J.; Samuel, D.; Selig, H.; Shamir, J. *Proc. Chem. Soc.* **1963**, 270.

(33) Tramšek, M.; Žemva, B. *J. Fluorine Chem.* **2006**, *127*, 1275−1284 (and references therein).

(34) Hoyer, S.; Emmler, T.; Seppelt, K. *J. Fluorine Chem.* **2006**, *127*, 1415−1422.

(35) Mootz, D.; Bartmann, K. *Z. Naturforsch., B: J. Chem. Sci.* **1991**, *46*, 1659−1663.

(36) Mootz, D.; Bartmann, K. *Angew. Chem., Int. Ed.* **1988**, *27*, 391−392.

(37) Bartlett, N.; Yeh, S.; Kourtakis, K.; Mallouk, T. *J. Fluorine Chem.* **1984**, *26*, 97−116.

(38) Shen, C.; Hagiwara, R.; Mallouk, T.; Bartlett, N. In *Inorganic Fluorine Chemistry, toward the 21st Century*; Thrasher, J. S., Strauss, S. H., Eds.; ACS Symposium Series 555; American Chemical Society: Washington, DC, 1994; Chapter 2, pp 26−39.

(39) Jenkins, H. D. B.; Tudela, D.; Glasser, L. *Inorg. Chem.* **2002**, *41*, 2364−2367.

(40) Jenkins, H. D. B.; Roobottom, H. K.; Passmore, J.; Glasser, L. *Inorg. Chem.* **1999**, *38*, 3609−3620.

(41) Gillespie, R. J.; Schrobilgen, G. J. *J. Chem. Soc., Chem. Commun.* **1977**, 595−597.

(42) Schrobilgen, G. J. *J. Chem. Soc., Chem. Commun.* **1988**, *22*, 1506−1508.

(43) *CRC Handbook of Chemistry and Physics*, 81st ed.; Lide, D. R., Ed.; CRC Press: Boca Raton, FL, 2000; Chapter 2, p 177.

(44) Dean, P. A. W.; Gillespie, R. J.; Hulme, R.; Humphreys, D. A. *J. Chem. Soc. A* **1971**, 341−346.

(45) Levy, H. A.; Burns, J. H.; Agron, P. A. *Science* **1963**, *139*, 1208−1209.

(46) Smith, G. L.; Mercier, H. P. A.; Schrobilgen, G. J. *Inorg. Chem.* **2007**, *46*, 1369−1378.

(47) Brock, D. S.; Casalis de Pury, J. J.; Mercier, H. P. A.; Schrobilgen, G. J.; Silvi, B. *J. Am. Chem. Soc.* **2010**, *132*, 3533−3542.

(48) Brock, D. S.; Casalis de Pury, J. J.; Mercier, H. P. A.; Schrobilgen, G. J.; Silvi, B. *Inorg. Chem.* **2010**, *49*, 6673−6689.

(49) Sundaraganesan, N.; Anand, B.; Meganathan, C.; Dominic Joshua, B.; Saleem, H. *Spectrochim. Acta, Part A* **2008**, *69*, 198−204.

(50) Bondi, A. *J. Phys. Chem.* **1964**, *68*, 441−451.

(51) Casteel, W. J., Jr.; Dixon, D. A.; Mercier, H. P. A.; Schrobilgen, G. J. *Inorg. Chem.* **1996**, *35*, 4310−4322.

(52) Emara, A. A. A.; Lehmann, J. F.; Schrobilgen, G. J. *J. Fluorine Chem.* **2005**, *126*, 1373−1376.

(53) Gillespie, R. J.; Landa, B. *Inorg. Chem.* **1973**, *12*, 1383−1389.

(54) Christe, K. O.; Schack, C. J.; Wilson, R. D. *Inorg. Chem.* **1975**, *14*, 2224−2230.

(55) Emara, A. A. A.; Schrobilgen, G. J. *Inorg. Chem.* **1992**, *31*, 1323−1332.

(56) Gerken, M.; Dixon, D. A.; Schrobilgen, G. J. *Inorg. Chem.* **2000**, *39*, 4244−4255.

(57) *APEX2*, release 2.0-2; Bruker AXS, Inc.: Madison, WI, 1995.

(58) Sheldrick, G. M. *SADABS (Siemens Area Detector Absorption Corrections)*, version 2.10; Siemens Analytical X-ray Instruments, Inc.: Madison, WI, 2004.

(59) Sheldrick, G. M. *SHELXTL-Plus*, release 6.14; Siemens Analytical X-ray Instruments, Inc.: Madison, WI, 2000−2003.

(60) Spek, A. L. *J. Appl. Crystallogr.* **2003**, *36*, 7−13.

(61) Basis sets and pseudopotentials were obtained from the Extensible Computational Chemistry Environment Basis Set Database, version 2/25/04, as developed and distributed by the Molecular Science Computing Facility, Environmental and Molecular Science Laboratory, which is part of the Pacific Northwest Laboratory, P.O. Box 999, Richland, WA 99352.

(62) Frisch, M. J.; et al. *Gaussian 03*, revision E.01; Gaussian, Inc.: Wallingford, CT, 2004.

(63) Frisch, M. J.; et al. *Gaussian 09*, revision B.01; Gaussian, Inc.: Wallingford, CT, 2010.

(64) *GaussView*, release 3.0; Gaussian Inc.: Pittsburgh, PA, 2003.

5104

dx.doi.org/10.1021/ja312493j | *J. Am. Chem. Soc.* 2013, 135, 5089−5104